Available online at www.sciencedirect.com
SCIENCE DIRECT®
Nuclear Instruments and Methods in Physics Research A 499 (2003) 437–468
NUCLEAR INSTRUMENTS & METHODS IN PHYSICS RESEARCH Section A
www.elsevier.com/locate/nima

The BRAHMS experiment at RHIC

M. Adamczyk[a], L. Antvorskov[b], K. Ashktorab[c], K. Asselta[c], E. Baker[c], I.G. Bearden[b], D. Beavis[c], C. Besliu[d], Y. Blyakhman[e], J. Brzychczyk[a], B. Budick[e], H. Bøggild[b], C. Chasman[c], C.H. Christensen[b], P. Christiansen[b], J. Cibor[f], R. Debbe[c], H. Diaz[c], L. Dutka[a], J. Engelhardt[b], J.J. Gaardhøje[b], K. Grotowski[a], K. Hagel[g,*], J. Hammond[c], J.C. Hansen[b], O. Hansen[b], A. Holm[b], A.K. Holme[h], H. Ito[i], E. Jakobsen[b], A. Jipa[d], J.I. Jørdre[j], F. Jundt[k], C.E. Jørgensen[b], M. Justice[c], M. Kajetanowicz[l], T. Keutgen[g], E.J. Kim[c,m], E. Kotula[a], T. Kozik[a], T.M. Larsen[h], N. Lindegaard[b], J.H. Lee[c], Y.K. Lee[m], G. Løvhøiden[h], Z. Majka[b], A. Makeev[g], E. McBreen[c], M. Murray[g], J. Natowitz[g], B.S. Nielsen[b], K. Olchanski[c], J. Olness[c], E.K. Olsen[b], D. Ouerdane[b], C. Pearson[c], K. Pena[a], D. Phillips[c], R. Płaneta[a], F. Rami[k], O.B. Rasmussen[b], D. Röhrich[j], B.H. Samset[h], S.J. Sanders[i], R.A. Scheetz[c], J. Sørensen[b], Z. Sosin[a], P. Staszel[b], T.F. Thorsteinsen[j,✠], T.S. Tveter[h], F. Videbæk[c], R. Wada[g], J. Westergaard[b], A. Wieloch[a], I.S. Zgura[d]

[a] *M. Smoluchowski Institute of Physics, Jagiellonian University, Kraków, Poland*
[b] *Niels Bohr Institute, University of Copenhagen, Denmark*
[c] *Brookhaven National Laboratory, Upton, NY 11973, USA*
[d] *University of Bucharest, Romania*
[e] *New York University, New York, NY 10003, USA*
[f] *H. Niewodniczanski Institute of Nuclear Physics, Kraków, Poland*
[g] *Cyclotron Institute, Texas A&M University, College Station, TX 77843, USA*
[h] *Department of Physics, University of Oslo, Oslo, Norway*
[i] *University of Kansas, Lawerence, KS 66045, USA*
[j] *Department of Physics, University of Bergen, Bergen, Norway*
[k] *Institut de Recherches Subatomiques, Université Louis Pasteur, Strasbourg, France*
[l] *Nowoczesna Elektronika, Kraków, Poland*
[m] *Johns Hopkins University, Baltimore, MD 21218, USA*

BRAHMS Collaboration

Abstract

The BRAHMS experiment at RHIC was conceived to pursue the understanding of nuclear matter under extreme conditions by detailed measurements of charged hadrons over the widest possible range of rapidity and transverse

*Corresponding author.
E-mail address: hagel@comp.tamu.edu (K. Hagel).
✠ Deceased.

0168-9002/03/$ - see front matter
doi:10.1016/S0168-9002(02)01949-6

momentum. The experiment consists of two spectrometers with complementary charged hadron detection capabilities as well as a series of global detectors for event characterization. A series of tracking detectors, time-of-flight arms and Cherenkov detectors enables momentum determination and particle identification over a wide range of rapidity and transverse momentum. Technical details and performance results are presented for the various detector subsystems. The performance of the entire system working together is shown to meet the goals of the experiment.

PACS: 12.38.Mh; 29.30.Aj; 21.65.+f

Keywords: Spectrometer; Relativistic Heavy ions; Particle ID

1. Introduction

The BRAHMS experiment was first proposed in 1991 as a "small" experiment at RHIC, and was subsequently approved for construction that started in 1997. The experiment was partly operational for the first RHIC beams in July 2000 and was completed for the 2001 run. The BRAHMS experiment pursues the understanding of properties of nuclear matter by detailed and precise measurements of charged hadrons over a large range of rapidity and transverse momentum. The present paper describes the design considerations for the experiment, the layout, construction and details of the individual detector components and the performance achieved for the different components.

2. BRAHMS physics goals

The BRAHMS detectors are designed to cover the widest possible range in polar angle relative to the beam direction with precise momentum determination and good particle identification (PID). In this way, the BRAHMS experiment will be complementary to the other three RHIC experiments that emphasize reaction angles near 90°, the mid-rapidity region. As angles of the measurements carried out approach the more forward angles, the laboratory momenta of particles increase from a few hundred MeV/c around 90° to 25–30 GeV/c around 2°. This led to the use of two separate spectrometers, one for low to medium momenta and one for high momenta, both with comparatively small solid angles. The actual sizes of the spectrometers are largely determined by practical considerations, such as the size and geometry of the experimental hall. The most forward angle achievable was set by the size and location of the RHIC DX magnets that control the beam intersection region and the dimensions of the beampipe. The BRAHMS spectrometer concept is an extension of the spectrometers used in AGS experiments E802 and E866 [1,2].

In characterizing particle spectroscopy at relativistic energies, it is customary to use kinematic variables that have simple properties under Lorentz transformation along the beam direction (boost transformations), rather than polar angle and momentum. Here we shall use two variables to describe the phase space of the observed particles: transverse momentum (p_t) and rapidity (y). p_t is defined as $p_t = p \sin\theta$ where p is the magnitude of momentum and θ the polar angle with respect to the beam direction; p_t is invariant under boost transformations. Rapidity is defined as $y = 1/2 \ln((E + p_{||})/(E - p_{||}))$, where E is the energy and $p_{||} = p \cos\theta$. Rapidity is additive under boost transformations and approaches parallel velocity divided by the vacuum velocity of light in the non-relativistic limit.

Fig. 1 shows the $y-p_t$ acceptance for π, K and protons in BRAHMS for the different spectrometer settings. Regions I and II in the figure show the regions accessible by the forward (high momentum) spectrometer (FS) and region III the range accessible to the mid-rapidity (low momentum) spectrometer (MRS). It should be noted that measurements in region III can be made simultaneously with those in any of the first two regions.

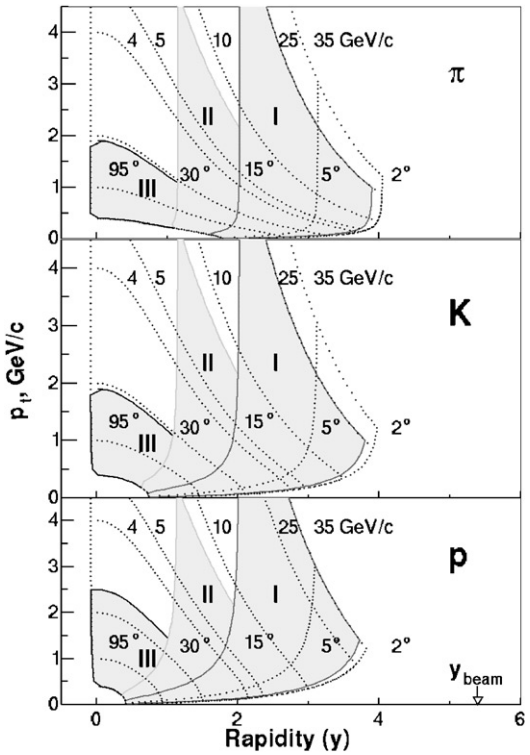

Fig. 1. BRAHMS acceptance for pions, kaons and protons. Region I and II show the acceptance of the FS with two different configurations, see below. Region III shows the acceptance for the MRS. The dotted curves marked 4, 5, 10, 25 and 35 GeV/c are curves of constant momentum, while the set marked 95°, 30°, 15°, 5°, 2° indicate curves at a constant polar angle. The fully drawn curves mark the acceptance borders.

The rapidity coverage of the entire spectrometer is from $y \approx 0$ to $y \approx 4$. For comparison the beam rapidity is 5.37 at the maximum RHIC collision energy of 100 GeV/u Au + Au. The other present RHIC experiments are limited to $|y| < 2$ for particle spectroscopy with good PID. The PID in BRAHMS utilizes standard spectrometer techniques, time-of-flight (TOF) (two systems in the FS and one in MRS), threshold Cherenkov and ring imaging Cherenkov detectors (both in FS). The p_t coverage is typical for soft collisions, but approaches the hard collision region (i.e. $y \sim 2-3$ and p_t up to 3–4 GeV/c) in region I.

Both spectrometers have small solid angles, 0.8 msr for the FS and 6.5 msr for the MRS; so the broad rapidity coverage is obtained by systematically combining many polar angles and magnetic field settings of both spectrometers. The BRAHMS detector measures averages over many events, and the events are characterized by a set of global detectors that can measure the charged particle multiplicity in a large solid angle near zero rapidity (the Tiles and Si detectors), the forward and backward charged multiplicities in a number of small solid angle Cherenkov detectors (the beam–beam counters (BBCs)) and finally neutrons near 0° with the zero degree calorimeters (ZDC). The ZDC calorimeters are common to all RHIC experiments.

The detector design enables the BRAHMS experiment to do hadron spectroscopy in a large rapidity and p_t range. The first goal of the experiment is to map out the rapidity density distributions for protons and antiprotons, a sensitive measurement for the dynamics of heavy ion collisions at these high energies. Other goals are the spectroscopy of pions and kaons as well as light clusters (e.g. deuterons and anti deuterons), all of which provide essential information on the reaction dynamics of the collision processes.

3. Experimental layout

A perspective view of the BRAHMS detector layout is presented in Fig. 2, where the two magnetic spectrometers, and the complementary global detectors are shown. The FS is positioned to the right of and near the beampipe at 2.3° and the MRS to the left of the beam-pipe near 90° from the perspective of beam particles traveling around the RHIC ring in the clockwise direction.

3.1. Forward spectrometer

The FS contains four dipole magnets, D1–D4, for sweeping and analyzing particles emerging from the reaction. D1 is of a septum design[1] in order to fit into the space near the beam pipe at the most forward setting of 2.3°. The maximum field

[1] Septum: a magnet incorporating a partition with a strong field on one side and little or no field on the other.

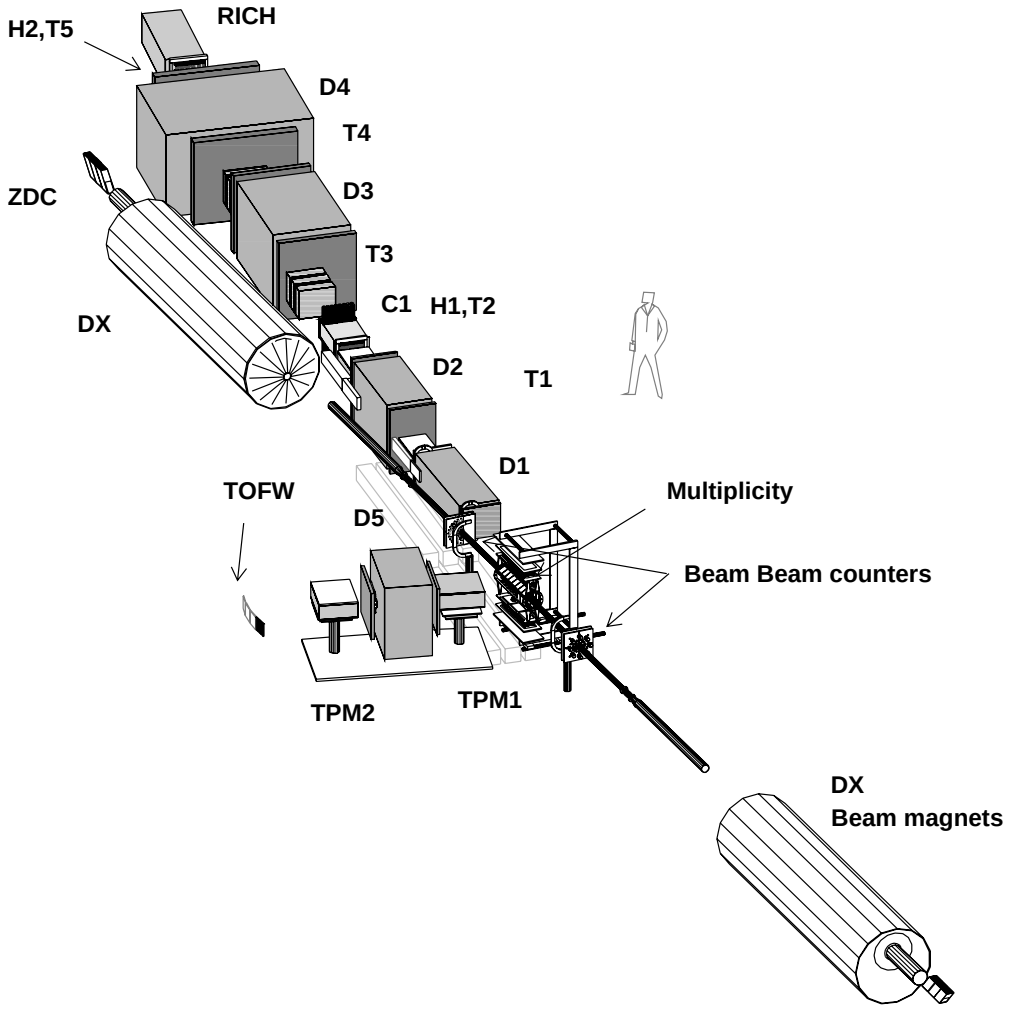

Fig. 2. The BRAHMS detectors in perspective. The spectrometer magnets are denoted D1–D5, the TOF hodoscopes in FS are H1 and H2, and the tracking counters T1–T5, where T1 and T2 are time projection chambers and T3, T4 and T5 are multi-wire DCs. The two Cherenkov counters in FS are C1 and RICH. The tracking chambers of the MRS are TPM1 and TPM2, while the TOF system is the TOFW. The global detectors are denoted as BBCs and multiplicity. The ZDCs are situated beyond the DX beam magnets. The distance between the front of the two DX beam magnets is 18 m.

in D1 is $B = 1.3\,\mathrm{T}$, enough to bend $25\,\mathrm{GeV}/c$ particles into the aperture of the subsequent magnet, D2. The magnets, D2–D4, are of conventional design. The FS has a solid angle of 0.8 msr.

The first two tracking detectors, T1 and T2, are Time Projection Chambers (TPCs) which provide good three-dimensional track recognition and a high degree of background rejection in a high multiplicity environment. The TPCs operate outside the magnetic fields and have a total drift distance of 21.8 cm. The remaining tracking detectors, T3–T5, are Drift Chambers (DCs) each consisting of three modules, where each module contains 10 planes for T3 and 8 planes for T4 and T5. A photograph of the FS is shown in Fig. 3.

The spectrometer can be operated in two configurations: one for the highest momenta and one for intermediate momenta. In the high

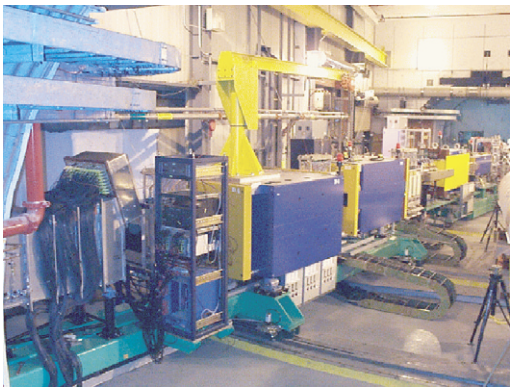

Fig. 3. The FS photographed from the far end towards the interaction region. The blue yokes of D3 and D4 appear in the middle of the picture. The rails for the high momentum configuration's movable platform can be seen. The RICH detector is to the left in the picture, while at the right side, the yellow yoke of D2 is visible.

momentum mode, particles are deflected by the dipoles D1 and D2 into the back end of the spectrometer where the tracking is performed by T2 and the DCs, and the momenta are determined by combining the tracking and the fields of dipole magnets D3 and D4.

In the intermediate momentum configuration, the particles are tracked by T1 and T2 and the momenta are determined using the field setting of D2. The D1–D2, T1–T2 part of the spectrometer, which constitutes the intermediate momentum configuration, is mounted on a platform that can rotate from 2.3° to 30°, while the high momentum configuration platform can rotate from 2.3° to 15°. In addition, T1, D2, T2 and H2 are mounted on a separate platform that can be rotated by an additional 3.5° relative to D1 to further reduce background rates at the most forward angles and lowest momentum settings.

Particle identification in the FS is based on two TOF hodoscopes, H1 and H2 and two Cherenkov detectors (C1 and ring imaging Cherenkov detector (RICH)). H1 and H2 consist of 40 and 32 plastic scintillator slats, respectively. Each scintillator is instrumented with two phototubes, one on either end. H1 is positioned 8.6 m from the nominal vertex and H2 is positioned 19 m from the nominal vertex. The TOF hodoscopes are designed so that π/K and K/p separation can be achieved to momenta of 3.3 and 5.7 GeV/c, respectively, for H1 and to 5.8 and 8.5 GeV/c, respectively, for H2. H1 and C1 are mounted on the intermediate momentum configuration platform, while the RICH detector is at the far end of the high momentum configuration. The threshold Cherenkov detector, C1 extends the $\pi/K/p$ identification behind H1 to 9 GeV/c while the RICH detector allows $\pi/K/p$ separation in the high momentum configuration up to $\sim$25 GeV/c.

3.2. Mid-rapidity spectrometer

The MRS is a single dipole magnetic spectrometer with a geometric acceptance of 6.5 msr and it covers the angular range of $30^\circ < \theta < 95^\circ$. The particle identification requirements are simpler in the MSR than in the FS because the typical particle momentum at the larger angles is lower. Only TOF is therefore used for this purpose. The D5 magnet in the MRS is placed between the two TPCs and has an aperture of $\sim 10 \times 35\,\mathrm{cm}^2$ at a distance of 1.9 m from the nominal vertex. Fig. 4 shows a photograph of the MRS.

Tracking in the MRS is done with the two TPCs (TPM1 and TPM2) which are similar in electrostatic design to the FS TPCs but different in general geometry. Particle identification is

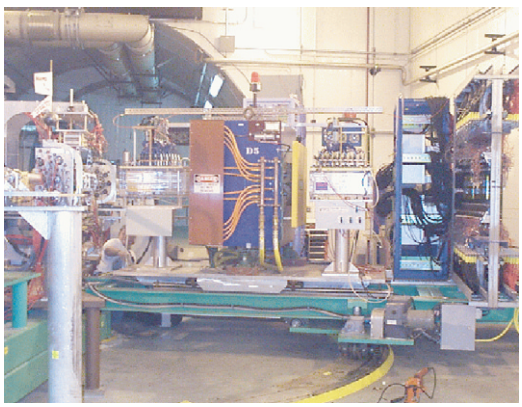

Fig. 4. The MRS. TPM1 and TPM2 are visible on the left and right, respectively, of the magnet D5. The TOF wall, TOFW, is visible on the far right. The nominal interaction vertex surrounded by the global detectors is visible on the far left.

accomplished with a highly segmented scintillator time-of-flight wall (TOFW) which provides π/K separation to momenta of 2 GeV/c and K/p separation to momenta of 3.5 GeV/c.

3.3. Global detectors

BRAHMS employs a series of detectors to enable event characterization by the observation of overall features of each detected collision, e.g. features that provide information on the collision centrality. Some of the detectors also provide signals for the first level triggers.

A two-component multiplicity array surrounds the interaction vertex (marked "multiplicity" in Fig. 2). The inner array is made of Si strip detectors arranged as a hexagonal barrel around the beam axis. The outer array of plastic scintillator tiles surrounds the silicon strip detectors, also mounted as a hexagonal barrel coaxial with the inner detector. This hybrid system measures the energy loss of charged particles that traverse the detector surfaces. Both arrays are segmented so that angular distributions can be obtained. By proper calibration of the Si and plastic detectors with minimum ionizing particles and use of detector simulation codes [3], it is possible to convert the energy loss data to event multiplicity within some systematic uncertainties, typically of the order 5–10%. The quantity of interest is the multiplicity as function of pseudo-rapidity, $dN/d\eta$, where the pseudo-rapidity is defined as

$$\eta = \tfrac{1}{2}\ln((p+p_{\parallel})/(p-p_{\parallel})) = -\ln(\tan(\theta/2)).$$

Pseudo-rapidity is a useful variable as it requires only knowledge of the polar angle and approaches rapidity at high momenta where momentum p approaches energy E. Given the geometry of the detectors as shown in the photograph in Fig. 5, the pseudo-rapidity coverage is $|\eta|<2.2$, corresponding to $12.6^\circ<\theta<167.4^\circ$, measured from the position of the nominal interaction vertex.

The BBCs are located on either side of the interaction vertex 220 cm from the nominal interaction vertex and very close to the beam pipe (see Fig. 2). They are constructed from two different-sized Cherenkov radiators glued to matching photomultiplier tubes (PMTs). The BBCs are positioned at pseudo-rapidities of 3.1, 3.4 and 3.6 relative to the nominal interaction vertex point. These counters provide a start time and a level 0 trigger. The 50 ps time resolution allows determination of the actual interaction vertex position to an accuracy of better than 1.5 cm from measurements of the difference in arrival times of the first particles to reach the two arrays.

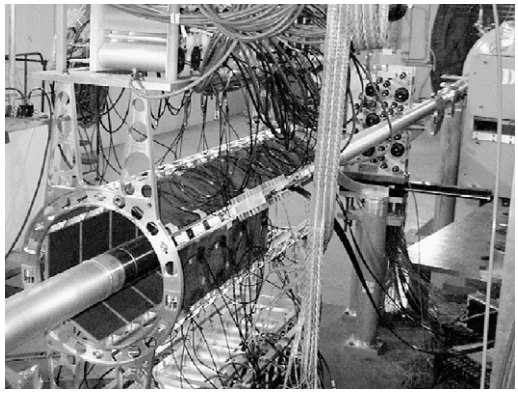

Fig. 5. Global detectors. The photo shows the hexagonal barrel arrangement of the plastic tiles (dark square surfaces), the beam line and to the right, just in front of the yellow yoke of the D1 magnet, one of the BBC arrays, where the radiators show as dark circles. The Si strip detectors have been removed for the picture and the other BBC array is outside the photo to the left.

The ZDCs [4] are placed behind the DX magnets on both sides of the interaction vertex 18 m from the nominal interaction point. They measure the total energy of neutrons in a cone of $\theta<2$ mr around the downstream beam directions. The ZDC resolution is 21% for one neutron at 65 GeV. Coincidence events in the two ZDC detectors provide a near minimum bias trigger, making it useful as an event trigger as well as a luminosity monitor [5]. In addition, the neutron multiplicity is also known to be correlated with the event geometry [6] and can therefore be used together with the data from the multiplicity array and the BBCs to estimate the centrality of the collision.

There are identical sets of ZDCs in all the RHIC experiments. They provide luminosity measurements for the RHIC machine group as well as neutron measurements. Since the ZDCs provide

some centrality information, the placement of identical detectors in all four of the RHIC experiments provides the possibility of comparing results from the different experiments obtained with nearly identical event characteristics.

4. BRAHMS subsystems

The various subsystems that make up BRAHMS are mounted on three movable platforms. The MRS is mounted on a platform that turns around a pivot point located vertically under the nominal interaction point. The D5 magnets and the two TPC detectors are mounted on a sliding plate on the MRS platform. This allows for increasing the distance to the nominal vertex and allows the spectrometer to be positioned to angles as forward as 20°. The D1 and D2 magnets with two TPC detectors (T1 and T2) plus the H1 hodoscope and the C1 Cherenkov counter are mounted on a second pivoted platform, while the high momentum part of the FS sits on a third platform that moves on two concentric rails. The reference marks for setting the platforms have a 1 mm diameter. Given the distances of the platforms from the nominal vertex, the angle settings of the MRS can be remotely controlled with an accuracy of 0.3 mr, the front portion of the Forward Spectrometer (FFS) can be controlled with an accuracy of 0.14 mr and the back portion of the Forward Spectrometer (BFS) can be controlled with an accuracy of better than 0.08 mr. The internal geometry of the spectrometer components on a platform is constant to better than 0.1 mm under any allowed rotation.

In the following, we discuss in detail the different subsystems which make up BRAHMS. Magnets are discussed first, followed by the detector subsystems, triggering data acquisition and online monitoring.

4.1. Magnets

BRAHMS has five dipole magnets, D1–D5, designed to provide momentum dispersion in the horizontal plane and momentum determination for the charged particles produced in the heavy ion collisions. The main requirements stem from the desire to cover as large an angular (rapidity) and momentum interval as possible with good momentum resolution. Limitations to meeting these requirements come from the multiplicity capability of the tracking detectors as well as the overall costs of the experiment. These requirements led to the design of an MRS magnet, D5, to be used alone for the lower momentum particles expected at mid-rapidity and an FS magnet array D1–D4, for providing the bend necessary for the higher momentum particles expected in the forward direction. With the exception of D4, the magnets are of the window frame design with the return yoke primarily on one side. This design was selected in order to secure the greatest forward angle coverage for the spectrometers. Typically, the maximum operating fields are close to 1.2 T, limited mostly by the stray field allowed on the RHIC ring.

The dimensions of the return yoke have been established by requiring that the iron thickness be one half of the horizontal gap plus a coil width multiplied by the ratio of the maximum field to 1.2 T. All magnets are thus slightly saturated at their maximum field. The dimensions of the coils and the size of the conductor are fixed by the available space, required Ampere-turns, and the requirements for cooling. The top and bottom coils are powered in series.

D1 is the most forward magnet and it is closest to the beam line. These conditions imposed two important design criteria. The first was that the magnet be designed to fit into the space near the beam pipe when placed at the most forward angle of 2.3° while delivering a field up to 1.3 T to give sufficient bending power to particles with momenta up to 25 GeV/c. The second criterion was that the design result in fringe fields of D1 small enough not to affect the beam optics when D1 is placed at the most forward angle of 2.3° with high field.

D1 has two "long" symmetric saddle (bed stand shaped) coils of 12 (3×4) turns each. The cross-section of the coils is $4 \times 4\,\mathrm{cm}^2$ and the dimensions of the magnet are given in Table 1. The magnet is designed to bend a particle with unit charge and momentum of 23.6 GeV/c 1.95° at 1.3 T. In order

Table 1
BRAHMS magnet parameters (all lengths are in cm)

	D1	D2	D3	D4	D5
Gap dimensions					
Height	8.0	13.5	25.4	32.0	10.16
Width	20.0	27.3	40.0	44.625	35.6
Length	200	160	200	183	76.2
Max. field (T)	1.26	1.68	1.22	1.19	1.45
$B\,\mathrm{d}l$ (Tm)	2.6	2.8	2.58	2.34	1.21
Current (A)	3450	3000	3000	2750	2500
Magnet dimensions					
Length	225	200.	253.3	251.5	99
Width	49.	98.	113.6	253.3	101.6
Shield thick	2.54	5.08	10.16	15.24	2.54

to minimize the distance between the magnet volume and the beam pipe (open side of the iron), the cross-section of the iron is designed to be "C"-shaped and the side nearest the beam pipe (open side of the iron) is closed with a 0.95 cm thick "septum plate" made of the same material as the magnet iron to reduce the fringe field at the beam pipe. The design of the magnet was optimized by the use of detailed three-dimensional field calculations using the code TOSCA [7].

The field vector outside the gap of D1 on the beam side of the magnet was scanned at a distance of 10.7 cm away from the septum plate along the length of the gap. For a mean field in the gap in the vertical direction (y-direction) was 1.2 T, the bending power of the y-component of the fringe field was measured in the scan to be $B\mathrm{d}l = 0.015$ Tm. The small strength of the fringe field has a negligible effect on the 100 GeV/c per nucleon beam.

TOSCA calculations were also used to calculate the fringe fields of D1. The results of these calculations are shown in Fig. 6 where we plot B_y versus x, the distance from the center of the magnet in the horizontal direction. At 23 cm, the distance of the beam pipe from the center of D1 when the spectrometer is placed at 2.3°, the fringe field of D1 is about 3 G for a center field of 1.3 T. This amount of fringe field poses no problems for the RHIC beam, consistent with the measurements discussed in the previous paragraph.

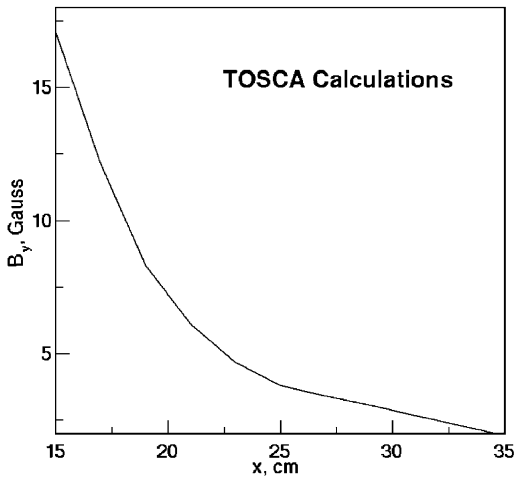

Fig. 6. TOSCA calculations showing the fringe fields in the y-direction as a function of the distance from the center of D1. The beam is at $x = 23$ cm when D1 is at 2.3°.

The magnetic field vectors in all the five dipole magnets were mapped in approximately 1 cm steps in three orthogonal directions, x, y and z, where x is the coordinate of horizontal displacement across the magnet gap, y is the vertical displacement and z runs along the length of the magnet gap. The mapping was done with a sensor containing three Hall probes mounted closely at the tip of a rod, and oriented in such a way as to read all the three components of the field. These probes were moved along a long rail with a micro-step motor in the z-direction. The displacement along

the x-coordinate was fixed by placing the long rail in holes 6.35 mm (1/3″) apart machined in bars mounted on the magnet shields. Raising these horizontal bars along four threaded bars changed the elevation or y-coordinate. The y-coordinate was measured with rulers having 254 μm divisions. Each magnet was mapped twice, one map at a half field and a second map at full field. During the mapping, the pitch and roll angles of the probe were recorded as well as the temperature at the probe holder.

Corrections for small probe rotations along the x-axis and planar Hall effect contributions to the small field components were corrected for in the off-line analysis by using the measured pitch and roll angles. Once the corrections were applied, an interpolation algorithm was used to produce a 1 cm^3 grid of field values inside the magnet gap. Fig. 7 shows an example of a field map of the x component of the field in D5 at half-maximum value.

The fields of D2–D5 were also modeled with TOSCA and excellent agreement between calculations and measurements were obtained.

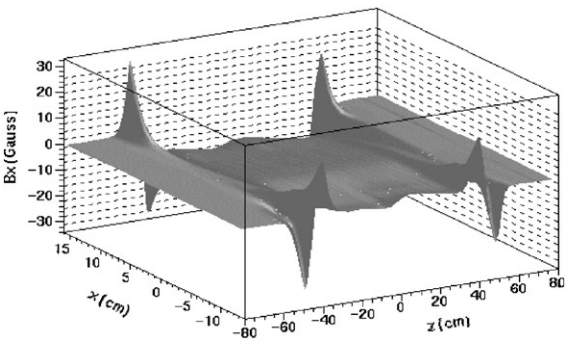

Fig. 7. D5 B_x component measured 1 cm above the medium plane ($y = 1$ cm). The measurements were made with an average field of half the maximum value.

4.2. Spectrometer detectors

4.2.1. Time projection chambers

TPCs are used as three-dimensional tracking detectors in both the FS and MRS. The TPCs were designed to achieve an intrinsic position resolution of better than 400 μm and a two-track resolution better than 15 mm. As the TPCs are placed outside magnetic fields, the tracks are straight lines. The particle multiplicities in each TPC, including secondary charged particles, are expected to range from 4 to 60 and the particle densities between 0.01 and 0.10 particles/cm^2.

Two TPCs are located in front (T1) and the back (T2) of the D2 magnet in the FS and the other two in front (TPM1) and behind (TPM2) the D5 magnet in the MRS (see Fig. 2).

The geometry of each of the four TPCs is adapted to its location. Table 2 summarizes the dimensions and other characteristics of those individual TPCs. T2 is built with two active volumes separated by a 5 cm spacing in a single field cage. The two readout planes each hold 8 pad rows separated by a 12.5 mm ground bus. Not all pad rows are instrumented in T1, T2, and TPM2, partly due to a desire to have one readout board per TPC, but also because track densities are such that sufficiently accurate measurements can be obtained with fewer instrumented rows.

The directions x, y and z used in Table 2 and throughout the paper, are defined as follows: y is in the direction of the main magnetic field (up), x is in the dispersive direction perpendicular to y and z is the length direction through the magnet, perpendicular to x and y.

Each TPC is contained in a Lucite box with two 25 μm mylar windows. Fig. 8 shows the TPM1 containment box with the field cage assembly.

Table 2
TPCs main characteristics

TPC	Dist. to vertex (cm)	Overall (x, y, z) cm^3	Active (x, y, z) cm^3	Pad rows	Pads per row	Pad size (mm^2)
T1	500	$45 \times 30 \times 70$	$33 \times 22 \times 56$	14	96	27.5×3
T2	810	$50 \times 30 \times 88$	$2 \times (39 \times 22 \times 31.5)$	2×8	112	27.5×3
TPM1	95	$67 \times 34 \times 67$	$37.5 \times 21 \times 36$	12	96	29.5×3.4
TPM2	285	$82 \times 30 \times 61$	$50 \times 22 \times 67.5$	20	144	24.5×4.2

In the TPC, electrons and ions are created from ionization by a charged particle passing through the gas volume. The primary electrons drift in the electrical field towards the read-out proportional chambers, i.e. upwards in Fig. 9. A minimum ionizing particle creates, on the average, ~90 electrons/cm. A uniform drift field gradient is guaranteed by field cages made out of a series of thin aluminized mylar strips (12 mm wide, 2 mm apart) connected to a resistor chain that linearly reduces the bottom cathode plate voltage at −5000 V to the ground potential near the read out plane (see Fig. 9). The figure also shows the gating grid which is discussed later. Extensive simulations have been performed during the design of the TPC field cages using the GARFIELD code [8]. As an example, Fig. 10 shows the calculated electric field lines together with the positions of the wire plane.

The choice of gas is determined by the relatively small size of the magnet gaps, which entails a short drift distance and therefore favors a slow gas. The mixture of 90% Ar and 10% CO_2 gas has been chosen for its slow drift velocity and low transverse (190 μm/cm$^{1/2}$) and longitudinal (240 μm/cm$^{1/2}$) diffusion constants. The TPC gas is fed to the chambers through individual mass flow meters used to adjust and regulate the gas flow. During operation, the average gas flow in each TPC is of the order of 500 ml/min and the gas

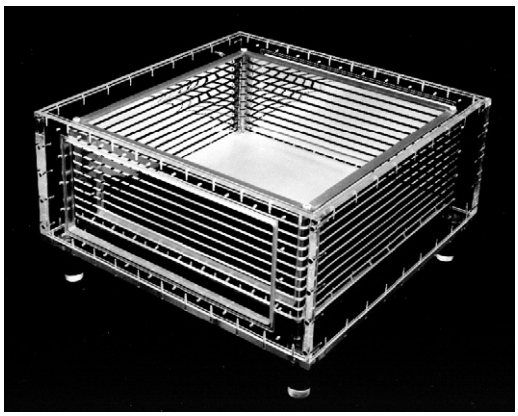

Fig. 8. TPM1 lucite box and field cage during construction.

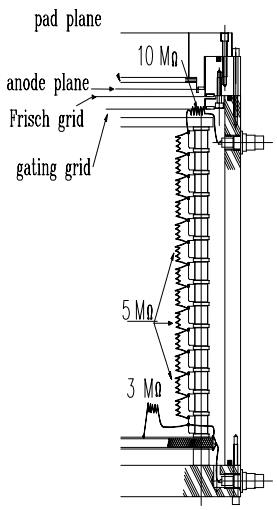

Fig. 9. Design of the field cage and resistor chain. The cathode plane is at the bottom of the figure and is held at −5000 V, while the anode plane, near the top, is at ground potential. See the text for further details.

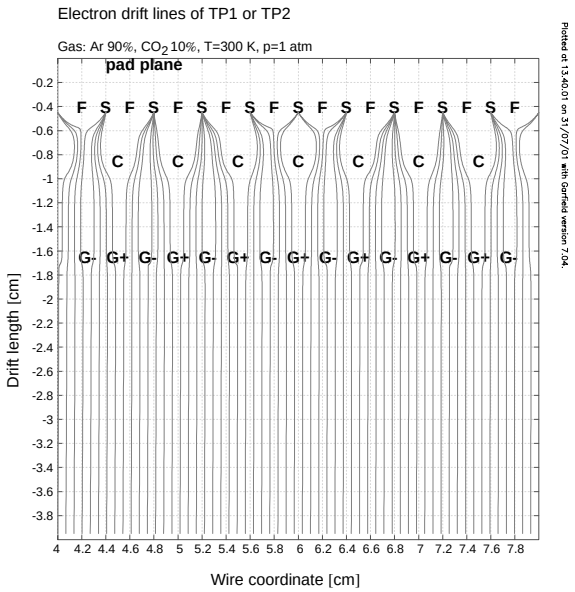

Fig. 10. Electric field lines near the TPC read-out chamber. All wires are perpendicular to the plane of the paper. The positions of the pad plane and the sense (S), field (F), cathode (C) and gating (G+,G−) wires are indicated. The cathode plane (C) is denoted as the Frisch grid in Fig. 9.

exhausts to the atmosphere with an overpressure of ~2 cm of mineral oil. With a 5000 V drop over a drift length of 21.8 cm, the field is 229 V/cm, yielding a drift velocity of 1.6 cm/μs with this gas.

A precise determination of the y-coordinate requires a precise knowledge of the drift velocity in the gas volume, a velocity that must be monitored continuously. This is achieved with drift velocity monitors installed in the gas system close to each TPC. Each monitor can measure the drift velocity of the gas mixture either as it enters the TPC or downstream of it. These monitors consist of a drift region in a small gas volume defined by alternating brass and G-10 frames. Each brass frame sits at a fixed potential defined by a resistor chain that runs along the length of the volume. Four slits cut in the G-10 spacers let electrons from an Sr source enter the drift volume. The slits are aligned in pairs separated by 1 cm. The drift region is connected to the grounded cylinder with an anode wire in its axis. The highest energy electrons from the two sources placed above the slits traverse the drift region and reach a scintillator located under it. The signal from the scintillator is the start of a FASTBUS TDC and the signal from the anode the stop. The drift velocity is determined from the time difference between the two peaks of the TDC distribution and the distance between slits.

The TPCs are read out by multiwire proportional chambers where the primary ionization electrons are multiplied through avalanche at the anode wires (sense wires) by a factor of ~10,000. Image charges are induced on an array of pads at a virtual ground potential located 4.5 mm above the sense wires. For each track segment, the drift time provides the y-coordinate, while the position and amplitude of the induced signals on the pad rows are used to extract the x- and z-coordinates. The pulse height of the induced signal on each pad, i, of an ionization cluster depends on the distance $(x - x_i)$ between the induced charge centroid, x, and the pad position, x_i. The resulting pulse height distribution, the Pad Response Function (PRF), is approximated by the Gaussian function:

$$P_i = A\mathrm{e}^{-(x-x_i)^2/2\sigma_x^2}$$

where the charge distribution width σ_x is a function of the drift length, the track angle and the transverse and longitudinal diffusion constants. The geometry of the pad plane has been chosen so that on the average, three to five pads collect the charges resulting from a primary ionization cluster.

The anode plane contains sense and adjacent field wires with a 2 mm (T1, T2) or 2.5 mm (TPM1, TPM2) pitch. A cathode grid (Frisch grid) at ground potential is placed 4.5 mm below the anode plane and a gating grid is located 8 mm below the cathode grid. Table 3 lists the characteristics of the various wires.

In order to have a TPC active only during well-defined collision events, a gating grid is installed between the Frisch grid and the drift region. In its closed state, the gating grid prevents positive ion feedback from the avalanche region near the sense wires into the drift volume. The gating grid is opened for about 20 μm by the event trigger. When open, all gating grid wires are at the same potential (−180 V). The closed state is obtained by applying different voltages to adjacent wires (−100 and −260 V), thereby creating an electrostatic field that renders the gate opaque to the passage of charged particles. The gating grid pulser circuit used to switch between the states follows closely the design developed for the NA49 and ALICE experiments [9]. Oscillations are minimized by adapting the pulser impedance to that of the HV cable and the TPCs. Special care was necessary to insure the best grounding of all connections to the TPC. All high voltage is set through filters that in practice are AC-grounds for high frequencies.

The charge collected on the TPC pads is amplified and integrated by a low-noise, low-input impedance charge-sensitive preamplifier followed by a shaping amplifier. The pulse height and the time history of the pad signal covering the maximal drift time are fed to a switched capacitor array analog memory clocked at 10 MHz. These

Table 3
Characteristics of the grid wires

	Sense	Field	Frisch	Gating
Material	W (Au plated)	CuBe	CuBe	CuBe
Wire diameter	13 μm	100 μm	50 μm	50 μm
Tension	15 g	150 g	100 g	100 g

Table 4
The resolution, averaged over rows, measured from track residuals

TPC	X (pad) μm	Y (time) μm
T1	380	396
T2	373	407
TPM1	310	427
TPM2	387	490

functions are achieved by the Front End Electronic cards obtained from the STAR collaboration [10]. Each card holds 2×16 preamplifiers and shaping amplifier channels and stores signal in 100 ns time bins.

The gating grid pulser and the readout board are triggered by a custom-built trigger/clock board as described in additional detail in data acquisition section.

The TPCs were tested with cosmic rays and the one-particle resolution averaged over rows is shown in Table 4.

4.2.2. Drift chambers

The DCs employed in BRAHMS will be described in detail elsewhere [11]; a brief overview is given below. The DCs were designed to achieve a position resolution of better than 300 μm FWHM as well as to allow the resolution of two tracks spaced more than 10 mm apart.

The FS employs three DCs, T3, T4 and T5, placed at 10.5, 14.5 and 18.4 m, respectively, from the nominal vertex. The detectors are designed to sustain the multiplicities expected at their respective positions, i.e. from 6 to 7 for T3 and somewhat less for T4 and T5. Therefore each module of T3 contains 10 detection planes and each module of T4 and T5 contains 8 detection planes. Each DC consists of three modules. The sense wires are spaced 1.0 cm apart in T3 and 2.2 cm apart in T4 and T5. The active areas of the DCs are $30 \times 40\,\mathrm{cm}^2$ for T3 and $35 \times 50\,\mathrm{cm}^2$ for both T4 and T5.

The wire directions are x, y, u, v, where the first two correspond to the x and y directions, where x is in the horizontal direction and y is in the vertical direction, while u and v are $+$ and -18° relative to the y-direction. Each x- and y-plane is followed by another plane with the same wire orientation, but shifted by a quarter cell width, to remove right–left ambiguities. Moreover, there are two x and two y planes in each module of the T3 detector. A detection plane consists of three frames made of epoxy-fiberglass. One frame contains the alternately ordered anode and cathode wires. Two frames with the field-shaping wires are placed on either side of the sense wire frame. The anode wire is gold-plated tungsten of 20 μm diameter stretched with 50 g tension. The cathode and field wires are made of beryllium–copper of 50 μm diameter stretched with 100 g tension.

The gas mixture employed is 67% Ar + 33% C_4H_{10}. A small quantity of ethanol is admixed by bubbling the gas through a bath of this liquid kept at 9°C.

The sense wire pulses pass through a coupling capacitor and are amplified and discriminated by the custom-made front-end electronics based on the ASD-8B integrated circuit developed at the University of Pennsylvania [12]. The ASD-8B is an 8-channel chip with differential inputs and outputs. Each channel consists of a charge preamplifier, shaper and discriminator. The boards are constructed in 16 and 8 channel versions based on the same printed circuit layout. The front-end boards are connected to the detector with 34 pin edge connectors. The differential output signal from the discriminator is connected to the 16-channel fast comparator board with regular twisted pair flat cables. The ECL standard driver outputs provide signals for the TDCs. To avoid output to input pickup, the comparators have been placed on separate boards. The ECL output pulses are fed to the LeCroy 1877S FASTBUS multihit pipeline TDCs on twisted pair cables and are used as the timing pulses. The common stop pulse for all the TDCs channels is obtained from the BRAHMS common LVL0 timing signal delayed by ~ 2 μs. In order to reduce the number of TDCs channels required, a multiplexer module is constructed. In this module, each pair of signals of two 16 channel inputs is combined onto a single line placing them there at different times separated by 400 ns. This multiplexing is used for the T4 and T5 DCs.

In Fig. 11 we present the single-particle position resolution from a prototype detector in a test run. The figure shows that the obtained value of 82 μm in the position resolution is much better than the design figure of 300 μm. Fig. 12 presents the photograph of T3 installed on the backward platform of the FS.

4.2.3. TOF systems

The particle identification (PID) in BRAHMS is performed in part by measuring the TOF of produced particles. Since BRAHMS is a collider experiment, one must determine the location of the collision as well as define a start time in order to extract meaningful PID from the TOF information. The start time and collision location are determined by the beam–beam array (see the subsection on BBCs below).

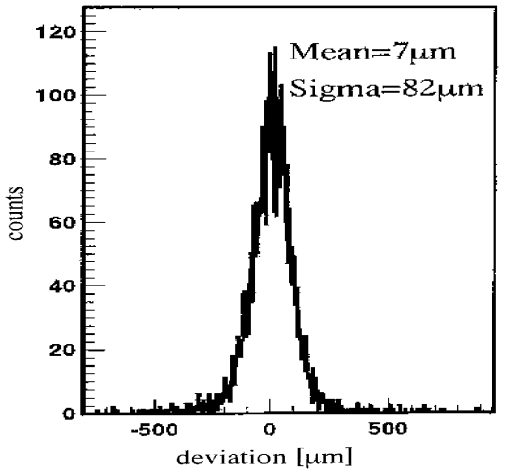

Fig. 11. One particle position resolution of the T3 prototype detector measured during a test run.

There are three TOF "walls" in BRAHMS, one in the MRS (TOFW) and two in the FS (H1 and H2). All the three are built of a number of vertical plastic scintillator "slats" read out by two Hamamatsu R3478 PMTs. One phototube is placed at either end of each slat. In TOFW, acrylic light pipes with a 30° bend direct the light to the PMTs. The bending direction alternates so that the tubes do not interfere and the tubes are coupled to the light pipe with 3 mm thick silicon "cookies" to allow for slight mechanical misalignments. In H1 and H2, the phototubes are attached directly to the two ends of the scintillator slat with optical grease and spring loading. Fig. 13 shows a photograph of TOFW mounted in place on the MRS platform.

Two signals are extracted from the base of each PMT, one is sent to a nearby Phillips 706 or 710 discriminator used to generate the timing signal, while the other signal, after a cable delay, enters a LeCroy 1885F FASTBUS ADC. The timing signals from the first discriminators are sent to the Fast Electronics Hut (FEH), where, after a second discrimination circuit followed by a delay line, they are recorded in a Phillips 7186 CAMAC TDC. The TDC is started by the common START and stopped by the individual signals from each PMT. The second set of discriminators, also Phillips 706 or 710, can also be used to provide

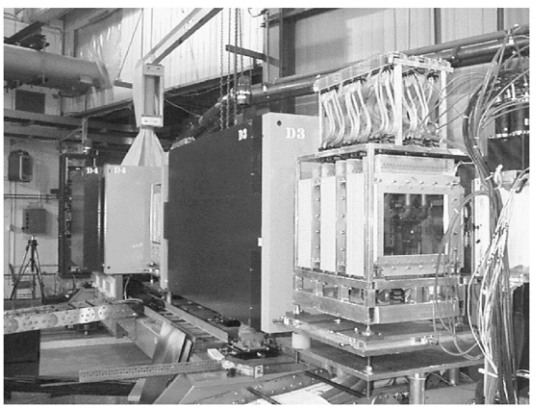

Fig. 12. T3 as installed in the forward spectrometer.

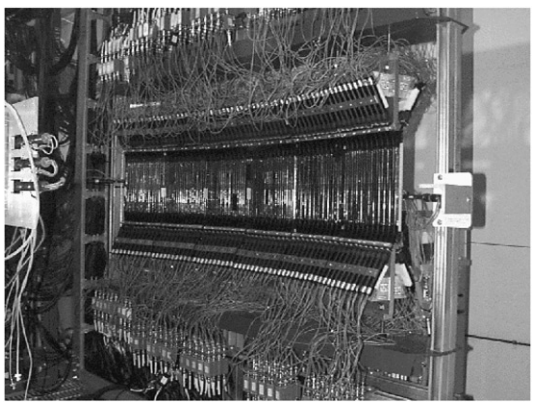

Fig. 13. MRS TOF wall.

signals to produce a hardware trigger on the number of hits in a given TOF wall.

The timing information is calibrated by summing a large number of events and assuming that the earliest peak in the resulting time spectrum is due to $\beta = 1$ pions. The intrinsic resolution of the individual slats has been measured in a test beam setup to be ≈ 65 ps. The in situ detector resolution is illustrated in Figs. 14 and 15 with data from typical slats in H1. Fig. 14 shows the difference in time measured in the top and bottom PMT, where it is required that the track hits the slat in one of three 1 cm regions in y. The peaks have $\sigma = 99$ ps. Neglecting the contribution due to the finite area over which the tracks hit, this implies a time resolution of 70 ps for each measurement. Fig. 15 displays the difference between the y position of extrapolated TPC tracks and the y positions calculated from the time difference between the top and bottom PMT and shows the position resolution obtainable from a typical slat. The broadness (RMS ≈ 1 cm) is primarily due to the timing resolution. It is noted that the position resolution is not good enough to contribute to the overall tracking, but provides unambiguous assignment of TOF hits to spectrometer tracks.

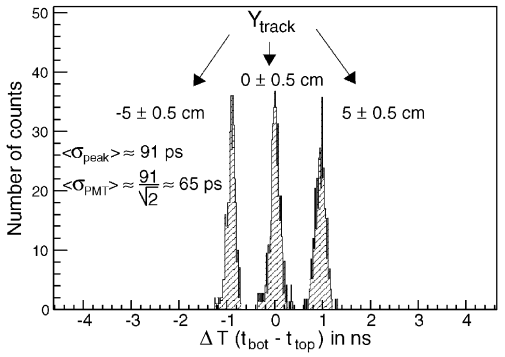

Fig. 14. Time difference between top and bottom in a typical H1 slat. Tracks are required to intersect one of three 1 cm regions along the length of the slat (y-direction).

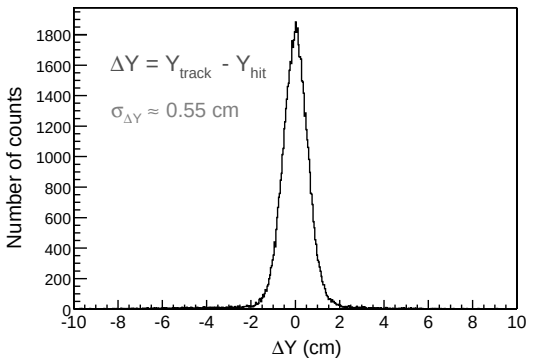

Fig. 15. Number of tracks in H1 plotted against the difference in the y-position of the extrapolated T2 track intersection with the slat, and the y-position in H1 calculated by the time difference (top–bottom) for all reconstructed tracks hitting the slat.

Table 5 summarizes the physical properties of the three TOF walls. In the first RHIC run, TOFW consisted of 83 slats, but has since been expanded to 125. The slats in TOFW are placed side-by-side along an arc with radius of curvature of 240 cm with the center located at the center of the D5 magnet, so that particles exiting D5 will have nearly normal incidence upon the individual slats. In H1 and H2, the slats are arranged in two staggered planes, with a 1 cm gap between each slat. This geometry allows full acceptance coverage with active scintillator, whereas placing the slats side by side would have necessitated a significant dead area due to the wrapping (Al foil and black plastic tape) of each slat.

As mentioned above, the particle identification does not depend solely on the timing resolution of the individual slats, but also depends on the resolution of the counters used to form the common START as well as the precision with

Table 5
Physical properties of the various TOF subsystems

	Location	Dist. to vertex (cm)	Number of slats	Slat dimensions $x \times y \times z$ (cm)	Material (bicron)
H1	FFS	860	40	$1 \times 20 \times 1$	BC420
H2	BFS	1890	32	$1 \times 40 \times 1.5$	BC420
TOFW	MRS	430	125	$1.27 \times 22 \times 1.25$	BC404

which one is able to reconstruct the position of the collision vertex and the subsequent track length through the spectrometer. The total TOF resolution before slewing corrections are applied has been found to be ~ 100 ps in both TOFW and H1. In the later section on spectrometer performance, we discuss the particle identification capability that we have achieved to date.

4.2.4. Cherenkov detectors

C1: C1 is a threshold Cherenkov detector installed as part of the front FS downstream of the H1 TOF hodoscope. It extends the particle identification obtained by H1. The detector has the pion threshold set at 2.6 GeV/c and it can discriminate between pions and kaons up to the kaon threshold at 9.3 GeV/c. It is not possible to discriminate between kaons and protons unambiguously between the limit of TOF discrimination (4σ cut) at 5.7 GeV/c and the kaon threshold of 9.3 GeV/c.

The Cherenkov detector design was kept as simple as possible. The radiator volume is 75 cm long, 50 cm wide and 40 cm tall and is filled with C_4F_{10} gas at atmospheric pressure. Cherenkov light produced by charged particles with momenta above threshold is reflected from two flat mirrors onto two photon detector planes above and below the radiator volume (see the schematic in Fig. 16). The photon detectors are closely packed arrays of 2″ diameter photomultipliers (Hamamatsu H1161) arranged in two rows of eight phototubes each. Light reflected by the flat mirrors is funneled into the active area of the PMTs by a set of glass mirrors arranged in the shape of a truncated pyramid. Fig. 17 shows this array of collimating mirrors seen from the entrance window of the detector as reflected in the two large mirrors. The number of photomultipliers defines the segmentation to first order. The cone of light that reaches the photon detector plane has a radius of ~ 6 cm and will shine on several cells. Tracking of the charged particles is necessary to extract the necessary particle identification information.

Entrance and exit windows are made with 25.4 μm (1 mil) aluminum foils mounted on the detector with O-rings. To fill the detector with the radiator gas, it was first placed in a filling vessel

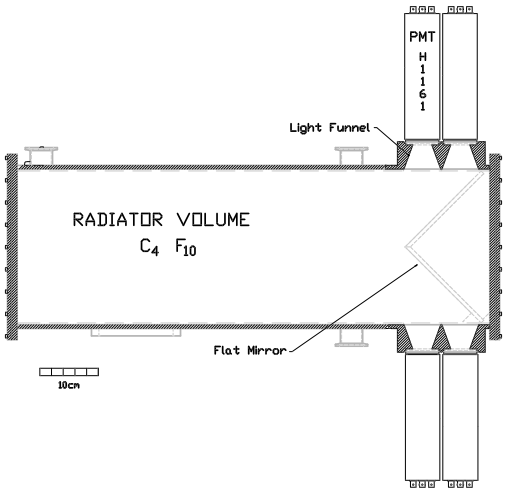

Fig. 16. Schematic side view of the Cherenkov detector C1. For details, see the text.

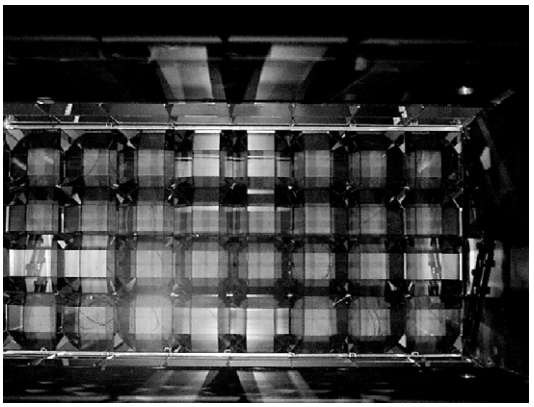

Fig. 17. A photograph of the mirror system of C1. The picture was taken from the entrance window. The reflection of the array of light funnels (Winston cones), that direct the light onto the PMT arrays, is clearly visible.

designed for this purpose. The filling vessel and the detector were then evacuated simultaneously while the pressure differential on the windows was constantly monitored. Once a good vacuum was reached, air was let into the filling vessel and C_4F_{10} into the detector. This filling procedure was done slowly while the pressure difference between the two volumes was maintained below 33 mbar.

The average index of refraction of C_4F_{10} for wave lengths within the photomultiplier dynamic range was measured with beams of momenta

ranging from 3 to 7 GeV/c. The value obtained was $(n-1) = 1380 \times 10^{-6}$, consistent with the threshold values above.

RICH: The identification of high momentum particles in the FS is done with the H2 TOF detector and the RICH detector (see Fig. 3). The RICH detector can identify pions with momenta starting at 2.5 GeV/c. Above 20 GeV/c, the ring radii of pions and kaons cannot be differentiated. Protons can be identified well above 30 GeV/c. The detector is situated in a low multiplicity environment of one or two tracks per event.

The RICH detector has a gas radiator volume of 8781 filled with a mixture of C_4F_{10} and C_5F_{12} at 1.25 atm. The Cherenkov light is focused onto a photon detector by a spherical mirror with a 3 m radius of curvature.

The photon detector is an array of 80 photomultipliers manufactured by Hamamatsu Photonics (model R7600 03 M4). Each PMT has four pixels for a total of 320 pixels. The PMTs are mounted in four bases that contain 20 tubes each, packed as closely as possible. The dead space between PMTs is about 2 mm. The active area of each pixel is a square 1.2 cm on a side. Each pixel on the photon detector has an amplifier because the PMT does not have enough gain to drive the FASTBUS ADC located in the Front End Electronics Hut. The amplifiers are IO-345 designed at BNL's Instrumentation Division.

The spherical mirror is rotated by 8° with respect to the spectrometer axis to focus the light onto the photon detector whose center is 16° off the axis and well shielded from charged particles that might cause background to the Cherenkov light. The photon detector is mounted behind a 25.4 mm (1″) thick quartz window 1.5 m from the center of the mirror.

The index of refraction of the radiator was set at 1.001850. Such a high index in a gas was obtained with a mixture of two perfluorocarbons: C_4F_{10} with a measured index of $n-1 = 1380 \times 10^{-6}$ at 1 atm and C_5F_{12} with a calculated value of $n-1 = 1620 \times 10^{-6}$ [14]. To fill the RICH, the radiator volume was first evacuated to a few milliTorr, while the entrance and exit windows were protected with end caps that allowed a vacuum on both sides of the windows. The first fluorocarbon to be introduced in the radiator was C_5F_{12} because at normal conditions it is a liquid. It was allowed to boil until it reached the necessary partial pressure of 630 Torr. Once that partial pressure was reached, the vessel was filled with pure C_4F_{10} to a pressure of 1.25 atm. The index of refraction was measured immediately after filling the detector using a Young interferometer that compares the optical path in two parallel tubes, one held at vacuum and the other filled with a sample taken from the detector. The interference fringes are detected with a PIN diode and counted with a PC after it is digitized in a Keithley's KNM-DC32. Prototype work for the RICH is described in Ref. [13].

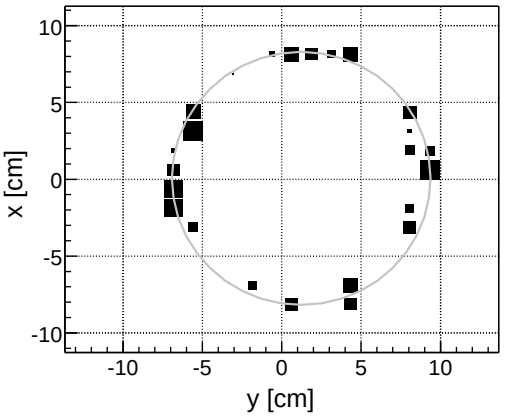

Fig. 18. An event with a ring detected in the RICH detector.

Fig. 18 demonstrates how the RICH detector is used in the analysis of higher momentum particles. The figure shows one event with a clear ring of at least 20 photoelectrons. This figure was made by making a correspondence between rings in the detector and tracks with momenta above threshold.

4.3. Global detectors

The global detectors include a multiplicity array composed of silicon strip detectors and scintillator tiles, a set of BBCs and a set of ZDCs to measure neutrons. A schematic of the arrangement of the multiplicity array and BBCs in relation to other elements of the spectrometer is shown in Fig. 19.

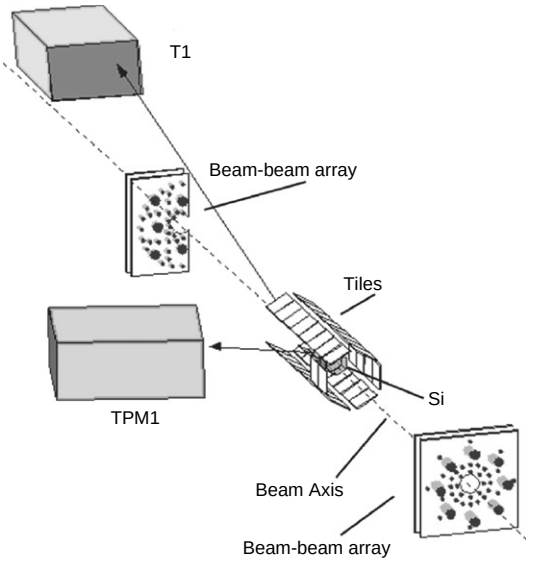

Fig. 19. Schematic depiction of the multiplicity array and beam–beam counters relative to other parts of the spectrometer. Recall that a photograph of the global detectors is shown in Fig. 5.

4.3.1. Multiplicity Array

The Multiplicity Array is used to establish overall charged particle multiplicities. An inner barrel of Si strip detectors and an outer barrel of plastic scintillator "tile" detectors measure the energy loss of particles passing through the array. The detectors are only modestly segmented in order to minimize the complexity and cost of the array. For a typical central collision, the segmentation results in multiple particles passing through individual elements. The number of particles passing through each element is determined by dividing the total energy observed in that element by the corresponding predicted average energy loss for a single particle as determined through GEANT simulations. This procedure works because there is a reasonably well-defined average energy loss for the charged particles emitted in a RHIC collision. The relationship between the measured multiplicities and the reaction centrality can be deduced based on model calculations and simulations of the array response. A pseudo-rapidity range of $-2.2<\eta<2.2$ is covered for collisions occurring at the center of the array.

A view of the Multiplicity Array mounted around the beam pipe is shown in Fig. 19 while Fig. 20 shows a picture of the Multiplicity Array without the beam pipe. All array elements are supported by an aluminum structure designed to have as little mass as possible and still preserve precision alignment of the detector elements. The support splits to allow for the removal of the array from around the beam pipe without having to remove individual array elements. The Si strip detectors are mounted close to the beam pipe in individual light-tight boxes. These, in turn, are suspended from the Al support frame by boxes containing the front-end electronics for the detectors. The plastic scintillator tiles are mounted directly onto the support frame.

During the year 2000 run period at RHIC, the inner barrel of Si strip detectors [15] consisted of 25, 4 cm × 6 cm × 300 μm wafers, each segmented into seven strips with a 0.86 cm pitch. The detectors were located 5.3 cm from the nominal beam axis. Both the Si strip detectors and scintillator tile detectors are arranged in hexagons about the beam axis. For the Si strip detectors, three rows were populated with six wafers each, covering 42 bins in pseudo-rapidity; one row was populated with five wafers, and two additional rows were populated with one wafer

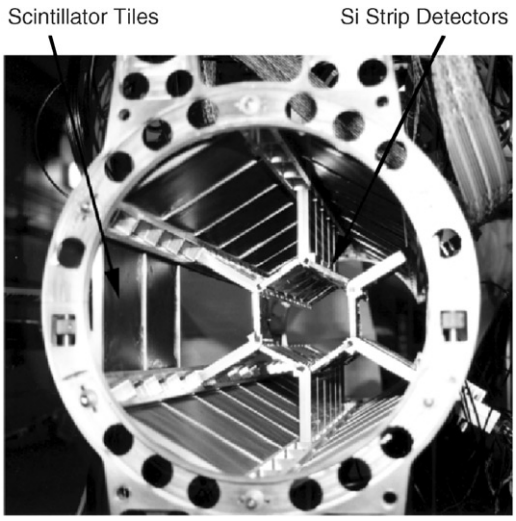

Fig. 20. Multiplicity Array with the Si strip and the scintillator tiles detectors. The beam pipe is not seen.

each, allowing one "ring" about the beam axis to be fully populated. The sparse population of two sides was to accommodate a clear line-of-sight for the two spectrometer arms and for reasons of cost. The discrete component front-end electronics located in the box supporting a given wafer contains seven independent preamplifier and shaping amplifier circuits. The amplified signals are transmitted from the Interaction Region (IR) to a remotely sited electronics room where they are processed, employing LeCroy 3309 peak-to-charge signal shapers and subsequent 11 bit FERA readout for the computer acquisition.

The outer detector barrel consisted of 38, $12\,\text{cm} \times 12\,\text{cm} \times 0.5\,\text{cm}$ tiles made of BICRON BC404 [16] scintillator connected by optical fibers to adjacent phototubes. The tiles were located at a distance of 13.9 cm from the nominal beam axis. Four rows were fully populated with eight detectors, each, one row had four detectors, and the last row had two detectors. These rows are partially populated in order not to obstruct the acceptance of both spectrometers. The tiles are independently wrapped with white bond paper and black Tedlar PVF file [17] before mounting onto the support frame. A 2 mm deep and 1.2 mm wide groove was machined along the edge of each tile to accommodate two turns of wavelength-shifting optical fiber. The fiber, of type K11 [18] is multiclad to increase light-trapping efficiency by 50% over conventional single clad fiber, achieving an acceptance light cone opening angle of 26° and a numerical aperture NA = 0.72. The diameter of the fiber was chosen as 0.83 mm to accommodate the required bending radius of 3 mm. Both ends of the optical fiber extend for a length of 75 cm out of the scintillators and are covered with a black light-tight jacket. The phototubes used for the tile array are Hamamatsu H3178-61 assemblies. The assembly is based on the 1.5 in. diameter tube R580-17 which has a green enhanced photocathode. Computer readout was done using dual-range FASTBUS ADCs located in the FEH.

The Si strip detectors and scintillator tiles give quasi-independent measurements of the event-by-event charged particle multiplicities allowing the two measurements to be averaged in the final determination of this quantity. The detectors also complement each other. The signals from the plastic scintillators are very fast and suitable for use in the first level "trigger" of the BRAHMS experiment. These detectors are also relatively inexpensive. The Si strip detectors have the advantage of greater segmentation, allowing 42 slices in η as compared to 8 for the tiles. The correction factor for secondary interactions, as deduced by the GEANT simulations, is also considerably less in the Si detectors, where it ranges from 6% to 30% of the total number of "hits" as compared to 20–40% for the scintillator tiles. The relatively high capacitance of the Si detectors makes it difficult to develop the fast signals necessary for the level 1 trigger circuit. In the geometry employed for the year 2000 experiment, the Si detectors subtended approximately 68% of the scintillator tile solid angle.

Fig. 21 shows the individual multiplicity distributions for the Si detectors and scintillator tiles as well as the correlation between the two. The difference in the extent of the number of hits for the two detector types reflects the different geometric acceptances. The different end-point

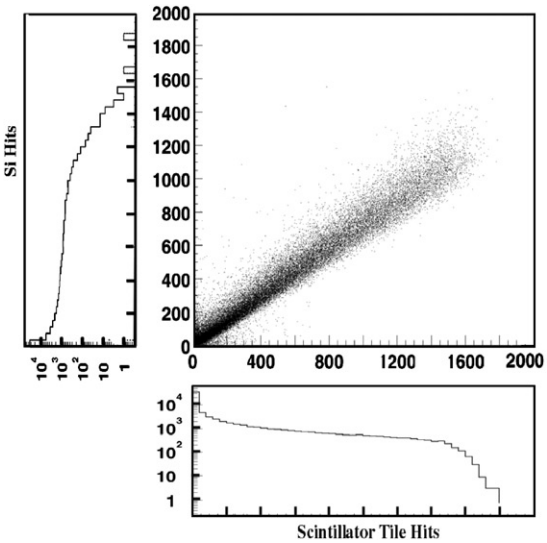

Fig. 21. Particle multiplicity distributions for the Si strip detectors and scintillator tiles. The multiplicity distribution measured by the Si strip detector is shown to the left in the figure and the corresponding scintillator tiles measurement at the bottom. The correlation of the two measurements is shown as the scatter plot in the middle.

behavior seen for the two multiplicity distributions can be attributed to differences in the Landau distributions of energy deposited in the Si and scintillator detectors and to a somewhat larger probability of electronics saturation for the scintillators. In general, however, a very strong correlation is seen between the two measurements.

4.3.2. Beam–beam counters

The BBCs are deployed to characterize collisions from a global perspective, to provide the zero level trigger, the start time for the TOF measurements, and to determine the primary collision vertex position to an accuracy of approximately 1 cm.

The BBCs consist of two arrays of Cherenkov detectors on each side of the interaction region. The design constraints of the system are dominated by the need to provide good start timing for the spectrometers. The modules are designed to detect Cherenkov light from $\beta \approx 1$ charged particles. The placement in a region of high pseudo-rapidity ensures that most particles have β near 1. However, this region has a high particle density, so that multiple particles striking a single module may compromise the ability to provide good timing. This problem is controlled by the use of two kinds of detector elements: one with a small enough geometrical solid angle; so the probability for multiple hits is small even for central collisions, and one with a much larger solid angle; so the probability of receiving at least one hit is large even for peripheral collisions.

The two arrays are placed at 220 cm on the left and right of the nominal interaction point. Fig. 22 shows the actual view of the two BBC arrays in the IR. The right array has reduced azimuthal coverage because the magnet D1 moves to within a few cm of the beam pipe when placed at the most forward angle. This reduced coverage is partially compensated by higher spatial density of modules in the array. The angular coverage is from 1.6° to 5.8°. Table 6 summarizes the details of the BBC characteristics and placements.

The small tube modules use a 3/4 in. Hamamatsu H5010 fast timing photomultipliers and the big tube modules utilize the 2 in. Hamamatsu R2083 tube. Each module has a Cherenkov lucite (UV transmitting) radiator, glued to the photomultiplier face. The length of the radiator is 4 and 3 cm for small and big tubes, respectively. In order to ensure both good timing and single hit response, this choice was made based on test beam studies.

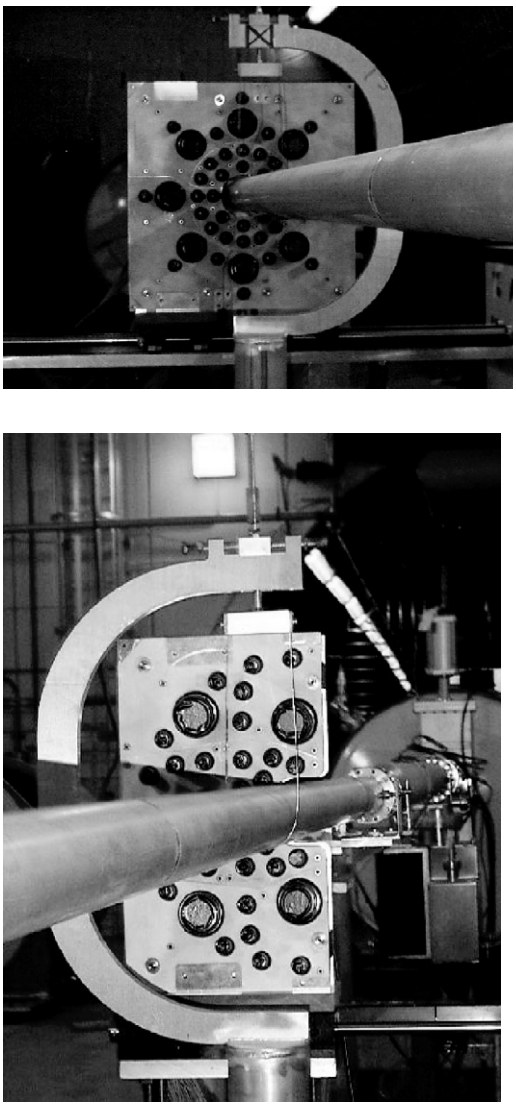

Fig. 22. The BBC array. The left BBC array is shown at the top and the right array at the bottom. The C-shape holder in the picture is part of the beam pipe support system placed ~30 cm in front of the BBC array. The large and the small solid angle elements are clearly distinguishable in the photo.

The Cherenkov radiator also provides some directionality selection since particles entering at

Table 6
Parameter details of the beam–beam counter arrays (all distances and sizes are in cm)

Array	Ring	Number of tubes in the ring	Radiator dist. from the beam	θ_{center}	η_{center}	Radiator length	Radiator radius
Left	1	8	6.5	1.7	4.2	4.0	0.95
	2	16	10.0	2.6	3.8	4.0	0.95
	3	4	14.9	3.9	3.4	4.0	0.95
	4	8	16.0	4.1	3.3	3.0	2.54
	5	8	21.5	5.6	3.0	4.0	0.95
Right	1	5	6.5	1.7	4.2	4.0	0.95
	2	4	8.3	2.2	4.0	4.0	0.95
	3	2	10.6	2.8	3.7	4.0	0.95
	4	3	12.6	3.3	3.5	3.0	2.54
	5	4	14.9	3.9	3.4	4.0	0.95
	6	4	18.5	4.8	3.2	4.0	0.95
	7	2	19.9	5.2	3.1	3.0	2.54
	8	11	21.5	5.6	3.0	4.0	0.95

large angles to the front surface or from the side and back give a much reduced signal. The left array consists of 44 modules made up of 36 small tubes and 8 big tubes, while the right array has 35 modules in total, with 30 small tubes and 5 big tubes (see Fig. 24). Each tube has two outputs. The signal from one output is fed to a timing discriminator situated close to the IR and the output NIM logic signal is sent on RG58 cable to the FEH, where it is regenerated and split in another discriminator. One of the split signals is used in the trigger and the other is sent as a stop signal to Phillips 7186 TDCs. The other output from the tube is sent, as an analog signal, directly to FASTBUS ADCs.

The prototype test was done using the secondary π beam at the AGS accelerator at Brookhaven. A demonstration of the performance is shown as the timing between a start counter and a large tube in Fig. 23. The signals have been corrected for time walk, and the combined timing resolution of ~ 75 ps demonstrates that the large tube detectors have an intrinsic resolution of ~ 60 ps.

The average time between a counter in the left array and one in the right array (or between a group in the left array and a group in the right) is a suitable time zero signal for the entire BRAHMS detector. In the limit where all the beam–beam detectors are considered to be on the beam axis and all particles detected to have velocity $\beta = 1$,

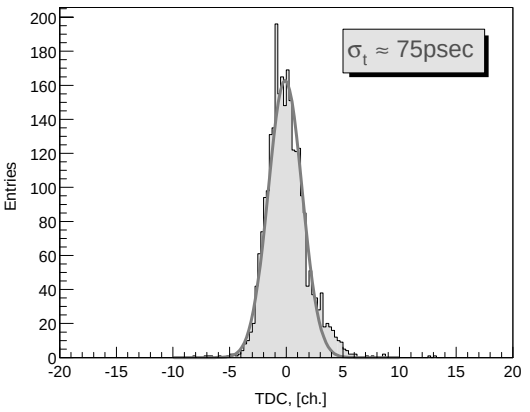

Fig. 23. Time distribution between a start detector and one of big tube counters in a test beam set up at the AGS (see the text for further details).

the average time of the right and left detectors is independent of the position of the primary collision vertex for any collision, since the sum of the two times equals the distance between the detector arrays divided by c, the speed of light. Thus the time zero signal is taken to be

$$T_0 = (t_{left} + t_{right})/2 + T_{const}$$

where t_{left} and t_{right} are the average times for a sample of left array and right array tubes, respectively and T_{const} is a constant time delay which depends on differences in cable lengths as

well as delay in different electronic modules. All times have been suitably corrected for walk (slewing correction) and all transit times through phototubes and cables have been measured and corrected for. The difference between left and right array times is a measure of the displacement along the beam axis of the primary collision vertex from the nominal vertex position,

$$z = c(t_{\text{left}} - t_{\text{right}})/2$$
$$= c((t_{\text{left}} - T_0) - (t_{\text{right}} - T_0))/2$$

where the right-hand expression can be constructed from the TDC results and from the corrections for transit times. The overall resulting uncertainty in the determination of the vertex from the BBCs is better than 1.6 cm.

The tubes also exhibit good multi-hit resolution. Fig. 24 shows a normalized ADC spectrum from minimum bias Au–Au collisions at 130 GeV for one of the 2″ big modules. Hits up to ~5 are clearly visible in the spectrum. It has been established by calibrations with a laser in a laboratory setup that the big modules have a linear response for the range of interest (up to 15 hits). The small tubes, however, exhibited non-linearity over the range of interest. Effort was made to calibrate out this non-linearity in the analysis. Examples of the use of the BBC arrays for the spectrometers (T_0 and z determination) and as a multiplicity detector are shown in the "Spectrometer Performance" section.

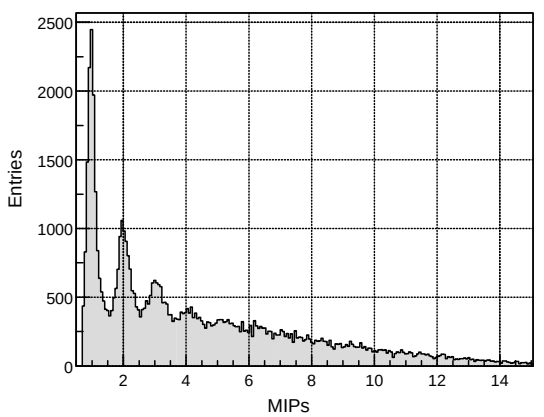

Fig. 24. Normalized BBC ADC spectrum for minimum bias Au–Au collisions obtained with a 2 in. tube.

4.3.3. ZDCs

The ZDCs are designed to measure the luminosity of the colliding beams. This capability allows the beam operators to tune the machine [4] and provides a means to compare results between different experiments. In addition, the time difference between the two ZDCs may be used to measure the position of the primary interaction vertex and to deduce the impact parameter of the event [6]. The BRAHMS experiment also uses the ZDCs to study the excitation of nuclei by virtual photons from the Coulomb field in extremely peripheral collisions [6]. Finally the pattern of energy and time signals from the individual modules in each ZDC allows the rejection of certain types of background events, a feature that will become increasingly important as the luminosity of RHIC increases.

High-energy collisions of nuclei usually lead to the emission by evaporation of spectator neutrons from both nuclei. At RHIC energies evaporation neutrons from spectators diverge by less than 2 mr from the beam axis. It is these neutrons which are detected by the ZDCs [4] when a collision occurs. In this "zero degree" region, the produced particles and other secondary particles deposit negligible energy when compared with that of beam fragmentation neutrons. The coincidence of both ZDCs serves as our minimum bias trigger and luminosity monitor [5]. The neutron multiplicity is also correlated with event geometry [6] and may be used to measure collision centrality. Since they are the only common detectors between the four RHIC experiments, cuts on the ZDC response provide a way to compare results among the RHIC experiments.

The calorimeters are positioned at a distance of 18 m from the nominal interaction point. Each calorimeter is divided into three modules, which is mechanically convenient and also allows a measurement of the energy deposition along the beam axis. This is a useful tool to discriminate against background particles entering the calorimeter from the back end. Since space is very limited, the ZDC use a very dense absorber, tungsten, and use quartz optical fibers to sample only the high-energy particles that produce Cherenkov light.

The difference in flight time from the vertex to each ZDC can be used to measure the vertex position while the average of the two times can be used as a time zero signal. After correction for the dependence of time on signal amplitude (time walk) a resolution of 170 ps is obtained. The resolution is dominated by the difference in path lengths of light from neutrons hitting the top or bottom of the ZDC. The timing resolution of both ZDCs leads to a ZDC vertex resolution of 3.6 cm. In general, the BBC array provides better time resolution and is used as the vertex position and time zero signal (see the previous section). In 2000 the distribution of vertices was approximately Gaussian with a width of 70 cm.

For particles hitting the ZDCs from the front, the first module should fire about 1.5 ns before the third module. For particles that hit the ZDCs from the back, the time difference is reversed. In BRAHMS this effect is used to reject background events caused by beam–gas collisions. The magnitude of the effect depends on the vacuum quality in the beam pipes in the BRAHMS interaction region. Typically only a small fraction of the energy in each event is deposited in the third module. Thus a large energy deposit in the third module is a sign that a particle may have hit the ZDC from the back.

From reactor tests at Texas A&M University, it was concluded that the optical fibers could tolerate a dose of more than 500 krad before needing to be replaced [4]. During the first year of RHIC running, the ZDCs showed no radiation damage. It is planned to measure the radiation dose with radiochemical monitors placed on the ZDC and to monitor for radiation damage by the position and width of the one neutron peak.

The ZDCs are also essential for the study of very peripheral events in which the nuclei do not touch but interact via an exchange of photons [6]. Such events are selected by requiring that there are no hits in the BBCs and the multiplicity array. In such events the energy absorbed by the nuclei causes neutrons (and some protons) to be emitted with very little transverse momentum. These neutrons can then be measured in the ZDCs. Since each nucleus interacts independently, we expect no correlation between the number of neutrons in the left and right ZDCs, a feature that is observed in the data. However, for nuclear events, the number of neutrons seen in each ZDC is correlated since spectator nucleons are produced from both colliding nuclei.

5. Trigger and data acquisition

At full luminosity the Au–Au nuclear collision rate is ~ 1.2 kHz of which about 10% are characterized as the most interesting central events with the highest number of tracks in the spectrometers. The distribution of collisions along the beam axis is expected to be Gaussian with an RMS of ~ 18 cm at the beginning of a fill and growing to ~ 25 cm over its lifetime of ~ 3 h with the 200 MHz re-bunching in place. The spectrometers are designed to accept particles with optimal acceptance when the vertex is within ± 15 cm of the nominal interaction vertex. The rate of central collisions within this acceptance is thus 60 Hz. The design criteria for triggering, readout electronics and DAQ capabilities is to be able to collect these central events, and a scaled down sample of other event classes with an overall data taking rate of ~ 100 Hz.

5.1. Trigger implementation

From a data acquisition point of view, the experiment consists of 12 detector systems that is comprised of about 500 channels of PMT, for which ADC as well as high-resolution TDC information is extracted, about 450 channels of PMT, for which only the ADC is read out, ~ 2500 channels of timing information from the DCs, and 160 ADC channels from the silicon array. By far the largest amount of data comes from the TPCs, which record up to 158 time bins of 10 bit ADC data from up to 1152 pads in each TPC. Apart from the customized readout of the TPCs, the experiment utilizes conventional CAMAC and FASTBUS modules for the digitization. It was also decided to implement the trigger system using NIM and CAMAC electronics, in part for reasons of cost, but also because all the readout systems impose fixed dead time, and the collision rates are

modest in heavy ion reactions. The design and timing were also driven by the decision to place most of the trigger and readout electronics in a trailer we call the FEH, placed just outside the shielding wall in the IR area.

There are two levels of triggers, denoted level 0 (LVL0) and level 1 (LVL1). LVL0 is defined as those triggers that gate the ADCs, TDCs, start the TPC gating grid and the readout cycle of the TPC Front End Electronics (FEE) cards. LVL1 is a trigger which subsequently interrupts the VME processors that handle the readout of CAMAC and FASTBUS modules. For the year 2000 running only LVL0 triggers were implemented. The triggers defining collisions come from two primary detector systems, namely the ZDC and the BBC. They are:

1. A left–right coincidence of the ZDC timing signals with a narrow time overlap of ~ 5 ns and with a summed energy signal from each module with energy > 25 GeV in coincidence with the RHIC RF clock signal.
2. A coincidence between the left and right arrays of the BBC with a requirement of two or more hits in a subset of Big Modules. A hit is defined as any analog signal that fires the discriminators set roughly at 40% of the signal recorded by one relativistic charged particle. The hits are selected from the big tubes (see the BBC section) at present, but the electronics allows for the selection of any subset of tubes to be involved in the decision.

The first trigger is the most inclusive selecting not only all nuclear reactions, but also the electromagnetic dissociation and peripheral collisions with the cross section of about 10.7 b [5]. The second trigger selects about 50% of the nuclear collision events. In the first RHIC run, these two triggers were sufficient to collect all data of interest, since the machine luminosity only reached 10% of the nominal value. Thus all LVL0 triggers also acted as LVL1 triggers.

In the 2001 run, a centrality trigger is implemented to select the 10% most central collisions with high efficiency. It is implemented by requiring a collision condition from basic BBC trigger, and then further requiring a large deposited energy in the Tile Multiplicity Array (TMA). This is implemented as a LVL0 trigger, and based on studies of data selects about 20–30% of all nuclear events, and all of the 10% most central events. A first level vertex selection is available for high luminosities based on making a precise cut on a timing overlap between the left and right ZDC modules (using Constant Fraction Discriminators) to accept only events with a narrow vertex of ± 40 cm. The combination of these allows to reduce the delivered interaction rate of up to ~ 1600 peripheral collisions to the rate of 100–150 events/s that the DAQ can handle.

The physical layout of the experiment, the trigger electronics and readout electronics result in a timing sequence with characteristics as shown in Table 7.

5.1.1. TPC readout

From each TPC up to 1152 pads each with 158 time bins are read out. The FEE [10] cards and readout board are electronics from the STAR experiment, procured as part of a collaborative agreement. The STAR FEE [10] cards digitize 512 time buckets, but the readout board was reprogrammed to only convert and transmit the first 158 buckets sufficient to cover the drift time of 13 μs in the four TPCs. The FEE cards connected on the detector each read 32 pads and is connected to a readout board. The readout-board is triggered from a trigger/clock module, and the digitized data is transferred from the board on a Giga-byte fiber Link connecting to a VME readout board. For a description of the FEE and readout board

Table 7
Trigger timing

	Time (ns)
Collision	0
BBC output	35
BBC at FEH	150
LVL0 input	320
LVL0 output	440
ADC, TDC gates	490
TPC readout start	1,030
TPC digitization start	12,000
TPC transfer complete	1,600,000

see Ref. [10]. The two other components are described in the following sub-sections.

5.1.2. Trigger clock module

The BRAHMS data acquisition (DAQ) is event driven and the TPC readout is activated through a special trigger/clock module that starts the readout cycle on the readout boards as well as supplies the clock signals for the Switched Capacitor Arrays (SCA). The trigger–clock module accepts up to three different external NIM inputs, corresponding to different trigger types. The input starts a sequence of reading a command word from a register, synchronizing the first cycles of the 10 MHz SCA clock to the command clock (RHIC 9.2 MHz RF clock), sending the appropriate command to the readout board and thus initiating the readout and digitization of the FEE cards. An output synchronized to the start of the SCA clock is sent to the TPCs and opens the gating grid. The synchronization is essential in reducing the RMS noise.

5.1.3. VME receiver module

The BRAHMS TPC receiver board is a VME based board that performs initial pedestal subtraction, pedestal suppression, and sorting of the TPC data. Each receiver board accommodates the data from one TPC and is interfaced to the readout board through a 1.5 GB/s fiber optical link. Data is transferred from the readout board to the receiver board at a rate of 20 bits every 34 ns using Hewlett-Packard GLINK transmitter and receivers.

The ADC conversion time dictates the maximum DAQ rate in the first step. For 158 time bins this amounts to 1.6 ms. Additional dead times are introduced when transferring data from the receiver board to VME processors, an amount that depends on the filling factors of the TPC. The charge from each time bin is digitized in 10 bit ADCs on the FEE cards. An important criterion was to make processing on the receiver board simple but fast, and postpone more sophisticated computations to the VME processors, that are programmable in C++. A dedicated VME processor board is interfaced to each receiver board, and performs reformatting of the data. The receiver board is therefore required to perform a "simple" pedestal subtraction, data ordering, pedestal suppression and clustering definition using CLPI chips and Field Programmable Gate Arrays (FPGA). The cluster algorithm is designed to keep two time bins above and below clusters, a cluster being defined as a sequence of 2 or more time bins with ADC values above their pedestal value. The data flow on the receiver board is shown in schematic form in Fig. 25.

The tasks performed by the BRAHMS receiver board can be divided into a 3-stage pipeline:

1. *Event readout*.
   Readout of the ADC data over the link: Data is read over the link at the rate of 20 bits of data and 4 bits of control information every 34 ns[2] by the optical receiver. The 20 bits of data corresponds to ADC values of 10 bits from two time pads. The control bits indicate if a transfer carries data or a special word. Consecutive data read over the link correspond to data from different pads with the pattern repeating itself for every 1152 pads for subsequent time bins.
2. *Data sorting and pedestal subtraction.*
   At this stage pedestal values are subtracted from the data, which are stored into static memory (SRAM) with 10 bits of data and two control bits indicating carry and overflow. The pedestal values and the addresses of where to store the ADC value from a given pad and time bin are kept in two r/w SRAM tables. It is noted that the pedestal value subtracted is the true pedestal for the ADC distribution for a given bin plus a threshold value. The threshold is added back to the subtracted ADC value in the VME processor. The processing is done at a rate of two words per 34 ns to keep up with the data being received over the link. It is done in four processing units, with one 10 bit word being fed into each unit once every ~ 68 ns.
   Upon the completion of event readout, the data that reside in the four SRAM data banks

[2] Both the design of the STAR readout board as well as the BRAHMS receiver board allows for twice this rate. When operating at that speed, though, the readout board experienced race conditions, causing additional noise in the data.

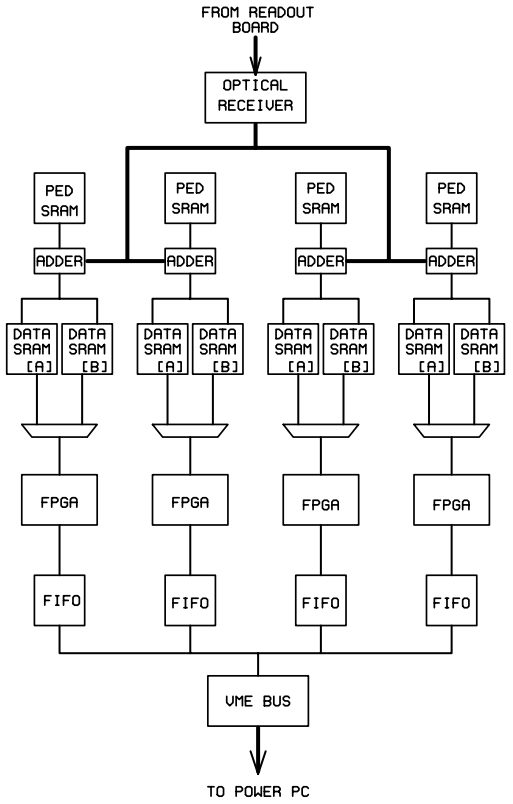

Fig. 25. Schematic diagram for the TPC VME receiver board. The components described further in the text are the pedestal and data SRAM, the FPGA and the FIFO.

are pedestal subtracted, sorted and consecutive memory locations hold data in time from the same pad. Each of these data banks consists of 256k of 12-bit memory. Two sets of the SRAM data banks exist, and alternate banks are used from one event to the next.

3. *Pedestal suppression and transfer to FIFO.*

Once the data has been buffered and if the previous event has been totally transferred to the receiver board the pedestal suppression stage starts. The receiver board has two complete sets of SRAM data banks allowing for suppression and transfer of one event while being ready to receive the next event. This stage consists of determining if the data are part of a "simple" cluster, tagging the beginning of the cluster and storing the data in FIFOs. Once a cluster is detected, the bins that constitute the cluster are written to a 8 k 16-bit FIFO together with a header and the data from the time bin preceding and the bin following the sequence. The FIFO is emptied by reading from the dedicated VME PPC2505 processor over a dedicated VME back plane using VME32 addressing block mode. The transfer rate is the limiting factor in the overall data-taking rate. For pedestal data where all time bins are read out, the limit is $\sim$10 events/s, while for typical data the limit is $\sim$150 events/s.

The VME processor has 64 Mb of local memory enough to keep a large number of events. The main task of the processor is to reformat the time ordered data. This reformatting is relatively simple, consisting in adding the threshold value back to the ADC values, and adding in each data sequence the row number, the pad number and the start time bin.

5.2. Data acquisition overview

The BRAHMS Data Acquisition is based on a distributed system of loosely coupled front-end processors that are interrupted by actions of the trigger systems, and a high-end workstation that serves the functions of event builder and user run control. The components and the performance are briefly described below. The architecture is illustrated by the flow of data in Fig. 26. The front-end VME processors initiate and interrupt the readout of data from the crates. The event fragments are buffered in local memory and transferred via a 100 MB Ethernet to a high-end Unix server, and the *event builder* program assembles a complete event. The server has a disk spool area capable of holding up to 100 Gb worth of data and acts as a buffer for the raw data files before they are sent, using the pftp protocol, via a Giga-bit link to the HPSS storage at the RHIC Computing Facility (RCF). The files on the spool area are also available via NFS mounting for rapid analysis from the workstations in the counting house. The DAQ design is fairly typical for a modern system, with the exception of the method employed for maintaining synchronization. This

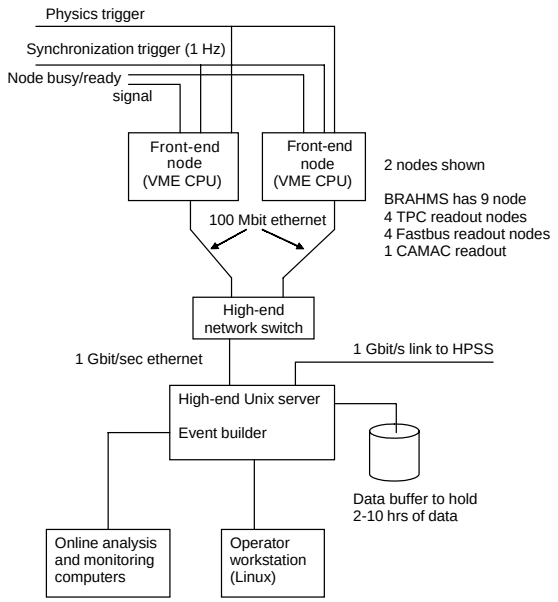

Fig. 26. BRAHMS DAQ data flow.

method is unique and is described below in some detail.

5.2.1. Hardware

All of the analog signals from PMTs are delayed via RG58 cables and fed to LeCroy 1885F 96 channel FASTBUS ADCs. The crate is controlled by a triple width STRUCK FASTBUS Interface (STR-340 SFI). The FASTBUS interface has up to four interrupts of which two are used by the trigger, one for physics events and one for synchronization events. The VME processor is situated in a two-slot dedicated VME back plane. A FASTBUS arrangement is used for the LeCroy 1877S pipeline TDCs that read out the DCs. The FASTBUS crate housing the DC readout is situated on the spectrometer platform.

The high-resolution timing signals from the TOF detectors, and the BBCs are read out by Phillips 7186 CAMAC TDC modules. Altogether six CAMAC crates in the experiment have Kinetics System 2132 Crate controllers connected to the SBE VME processors [19], which in turn are controlled by another MVME 2305 or MVME 2307. The VME processors all run under the VXWorks embedded operating system.

The Unix server is a six-processor SUN E3500 running Solaris 8 and has attached 100 Gb of disk with the main function of serving as a spool buffer for the raw data before these are sent to RCF. The network connection used for sending raw data to RCF is a dedicated GB fiber network utilizing jumbo frame to allow for maximum data rate.

5.2.2. Software

The DAQ software is also distributed across the processors. The time-critical software sits on the front-end VME processors, the time-critical synchronization is done via the trigger logic by interrupts for the beginning of an event, and by setting a ready level when completed. The next level of software runs on the Unix server. This consists of two main components, namely the *event builder* (I/O server) and the *runcontrol* program that is responsible for all command communication between the distributed processors, and the I/O server and the user control interface. Each of these components is described in some detail below.

5.2.3. Event builder components (I/O server)

The event builder has several major components, most of them implemented as threads inside the event builder process. The receiver checks data validity, creates the event fragments and passes them to the event assembler, which matches them into complete events. A data mapper receives assembled events and creates the mapped data records. This process does not perform any re-mapping of the data. An output manager takes and distributes them to output data streams on disk, net connections and possible local tape.

5.2.4. Event synchronization

An important issue in a loosely coupled distributed system is to ensure data integrity and synchronization. This is achieved in the present system, by having the trigger system set up synchronization events that causes the front-end processors to tag this sub-event as having a different data type. These are presently set at a rate of 1 Hz, with typical 100 physics events

between each occurrence. The synchronization trigger causes a separate interrupt of the VME processors. In the case of the TPC readout, this is indicated by the 'DAQ' word sent to the TPC readout board from the trigger/clock module. If the event builder sees a mismatch, i.e. the data fragments do not all correspond to such a synchronization trigger, it will reset the data taking via a command to the run-server, and will discard all events from the previous accepted synchronization event. Such failures are rarely observed. When they do occur, it is typically due to loss of a single front end node, e.g. from a power failure or a startup after configuration changes have taken place.

5.2.5. *Run server*

The main purpose of a separate run server program is to provide a well-defined interface between the logic part of run control, implemented as a state machine, and the user part of run control. The run server interface is defined by an IDL interface that contains methods to initiate run state transitions, such as "begin run" or "end run", and methods to query the run server for information, such as run state, run number, etc. By calling the control methods defined in the run server interface a run control program can cause state transitions in the run server. During a state transition, the state machine issues commands to the front-end nodes and the event builder causing them to start or stop taking data. In addition to reacting to user interface commands, the run server has a background task to poll the front-end nodes and the event builder for information. The background task performs check on the collected data and, if necessary, can force state transitions or initiate other actions and change the run state.

The user interface to the run control is a graphics interface implemented in Java. This interface is running on local Linux workstations in the counting house. In addition to the normal tasks of defining configurations for run, starting and ending runs, it gives the user access to details of events, front-end node activities, log files, etc. Configuration changes, and run conditions are recorded in a local MySQL database.

5.2.6. *Performance*

The DAQ system, for FASTBUS and CAMAC readout alone, is capable of handling up to 1000 events/s, equivalent to 20 Mb/s. For complete physics events, the limits are about 500 events/s as set by the TPC readout board. It may be further reduced depending on the amount of data after pedestal suppression on the TPC receiver board.

During the final weeks of the 2000 run, the maximum collision rate at the BRAHMS IR was about 200 Hz. The data-taking rate was $\sim$100 Hz with an average event size of 60 kb and dead times of $\sim$60–70%. The event size was higher than anticipated, mainly due to a large number of clusters in the TPM1 the one nearest the IP. The amount of data recorded in this fairly short run was about 2 Tb. During the 2001 run, the experiment recorded about 17 Tb at average rates of about 60 events/s.

6. Online monitoring

Online monitoring in BRAHMS is accomplished using a variety of methods and software. All of the BRAHMS monitoring software is based on the ROOT [20] program. One piece of software is a monitoring program, which samples data from the event builder and increments the various diagnostics spectra generated by the selected detector groups. The generation of a ROOT tree [20] from a subset of data, right after a particular run was completed, was found to provide a rather powerful near real-time analysis method. The TPC tracking performance was monitored separately by sampling the TPC data and plotting various projections of the pad hits and time distributions.

6.1. *Monitoring program*

The program to monitor BRAHMS data online has three components. The components consist of monitor modules, a "super-module", which acts as a manager of the monitor modules, and a main program which creates the "super-module" and adds all of the monitor modules depending on which switches the user sets at startup.

The primary component is the monitoring module, designed to work standalone in ROOT or to be added to a "super-module". The monitoring module as presented to the operator has two lists that can be clicked on to display either a single histogram or a set of histograms, which we call a picture. In addition to these lists, there are buttons to control input of the data from the event builder or from a raw data file as well as to clear arrays or to integrate the contents of one dimensional or two dimensional histograms.

The component used most often in the experiment is a "super-module" which has the capability of loading a number of the monitoring modules and keeps track of them in a list. It also has a number of buttons to control event input from the event builder or raw data file as well as a number of "global" operations such as clearing all arrays of loaded modules. Once a particular detector module is loaded, its array-incrementing routines are executed event by event. The arrays and pictures for each detector module are presented to the operator as tabs in the main operator console. Once a detector module is selected, the list of defined arrays and pictures for that module are presented to the user. In addition, buttons for each monitor become visible which operate only on the data for that particular monitor.

The third component is a program that can be executed by the user to create the "super-module" and add the different detector modules according to switches set in the command argument. There are typically several of these programs with different combinations of detector monitoring running on different nodes.

6.2. Tree program

A program was written to transform the raw data into some simple structures, useful for monitoring and diagnostics, structures that were written in a ROOT Tree and therefore could be read back and used for analysis. This added analysis capability was found quite powerful, in that spectra with different gates could be generated very quickly as the need arose.

The program is similar in spirit to the monitoring program. There is a base class which handles all of the complex ROOT features and inherited classes that perform the detector specific work to extract the proper data from the raw data stream and transform it into the ROOT Tree structures. A main program creates all the elements and adds them to a list and then executes the data generating routine on an event by event basis.

6.3. 3D monitoring of TPCs

It is very important to have a graphics view of the performance of a TPC. Many problems were diagnosed by looking at track patterns from various samples of events. A program was developed which read in the raw data, extracted the TPC information and made pictures of the pad hits. Both projections of the pad hits as well as 3D representations of the tracks were generated. Fig. 27 shows an example of the TPC viewer used during the run. The left panels from top to bottom show the $x-z$, $y-z$ and $x-y$ projections, respectively. The right plot shows a 3D

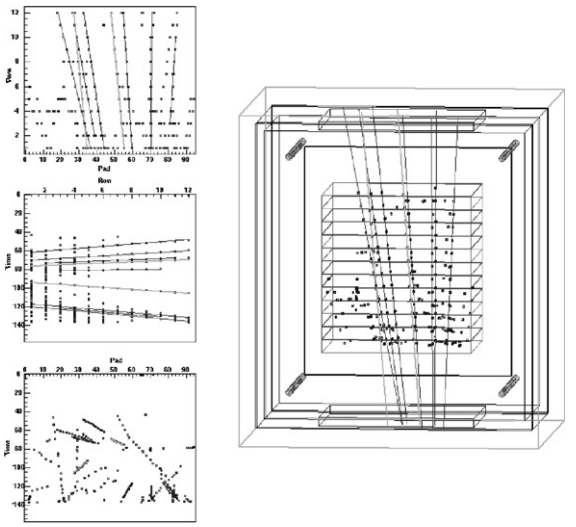

Fig. 27. Online event viewed with the TPC 3D viewer (see the text for further explanation). The top left panel has the x-axis as the pad number and the y-axis as the row number (i.e. a projection of the tracks onto x–z). The middle left panel has the x-axis as the row number and the y-axis as the time (i.e. a projection of the tracks onto y–z. The bottom left panel shows a projection of the tracks onto x–y, the pad number on the x-axis and the time on the y-axis. Finally the right panel shows the 3D image of the tracks which is rotatable.

representation of the track through the TPC. The 3D representations of the tracks can be rotated to achieve better views of the tracks.

In addition, clicking on a pad in one of the projected views would generate 1D histograms of time, pad or row depending on the selected projection. The program presents the user with a series of tabs each of which has plots and information regarding a different TPC.

7. Spectrometer performance

Any collider experiment presents the challenge of determining where a particular collision between a particle from one beam with one from the other beam occurs. The precise determination of the collision vertex is important for several reasons. First of all, the distance a particle travels to the respective detectors depends on the position of the collision vertex and therefore is essential for particle identification by TOF. In addition, the acceptances of the spectrometers vary with the position of the collision vertex as does the determination of the polar angle of the particle momentum.

As noted above, BRAHMS has three detector systems with vertex position determination capabilities, the BBCs, the ZDCs and the MRS TPM1. The BBC array and ZDCs provide a determination of the vertex position by a measurement of the difference in arrival times of particles that hit the left and the right detectors of each one of the systems, while the vertex determination from the TPM1 is achieved by projecting the identified tracks to the nominal beam axis. Fig. 28 shows the correlation of the vertex determined from TPC tracking with the one from ZDC timing. An excellent correlation between the two determinations is apparent.

The multiplicity array combined with the BBCs cover the pseudo-rapidity range from -4.3 to $+4.3$ and provides a rather complete measurement of the angular distribution of charged particles emitted from a heavy ion collision. The three detector types involved do not measure number of particles directly: the Si strip detectors and the scintillator tiles measure energy loss, while the beam–beam detectors measure Cherenkov light. By appropriate normalization to the average energy loss in each detector element and careful simulations, the signals from the multiplicity array can be translated into number of hits on a statistical basis. The light spectra from the BBCs, as shown in Fig. 24, carry the needed multi-hit information to also yield the received number of hits. An example of $dn/d\eta$ distributions obtained from central Au + Au collision at a center of mass energy of 130 A GeV is demonstrated in Fig. 29, taken from Ref. [21].

Particle identification is achieved by the use of the momentum measurement obtained with the tracking through two TPCs with a dipole magnet in between and the data from the TOF arrays located behind the tracking detectors. As noted above, the particle identification is dependent upon an accurate determination of the collision vertex.

Fig. 30 presents an example of the measured TOF versus momentum of positively charged particles from Au + Au reactions at 200 GeV/u obtained in the MRS during the 2001 run. Pions and kaons are clearly resolved up to 2.2 GeV/c and kaons and protons up to 3.5 GeV/c.

For H1 in the FS, the situation is slightly more difficult since the particle momenta are much larger and the path length more dependent upon

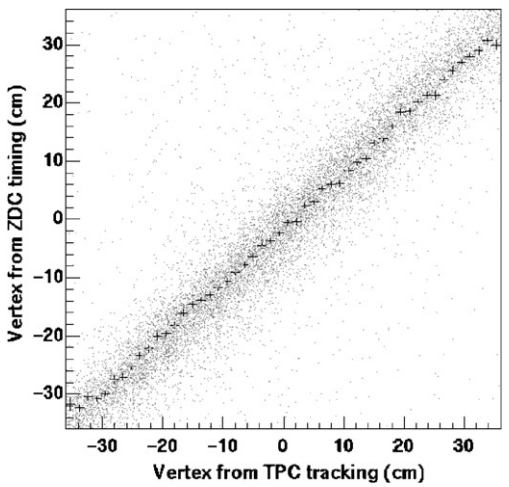

Fig. 28. Correlation between vertex determination from the ZDCs and the TPM1 time projection chamber.

the vertex position than is the case for the MRS. The contribution of the uncertainty in the vertex position Δz to the path length is $\Delta l = \Delta z/\cos\theta$. At an angle of 4° in the FS, an uncertainty in the vertex position of 1 cm corresponds to a timing uncertainty of 30 ps for particles with $\beta = 1$. A TOF versus momentum plot for positively charged particles is shown in Fig. 31 for the reaction angle of 20°. Pion and kaon separation is achieved in a narrow momentum interval below 3.0 GeV/c, while the protons are separated from π and K up to 5.2 GeV/c. The measurements are described in detail in Ref. [22] using the TOF particle identification for the 2000 run.

The PID at somewhat higher momenta is achieved by adding the information from the C1 Cherenkov detector and provides π/K separation in the momentum range of $3 < p < 9$ GeV/c. Fig. 32 shows a preliminary response of the C1 vs mass^2 as determined from the TOF and mass measurements at a forward angle of 4°. The pions in the energy range $3 < p < 9$ GeV/c (above $p = 3$ GeV/c) give a significant signal in the C1 while the kaons and protons do not.

With the full implementation of the backward portion of the Forward Spectrometer (BFS) in the

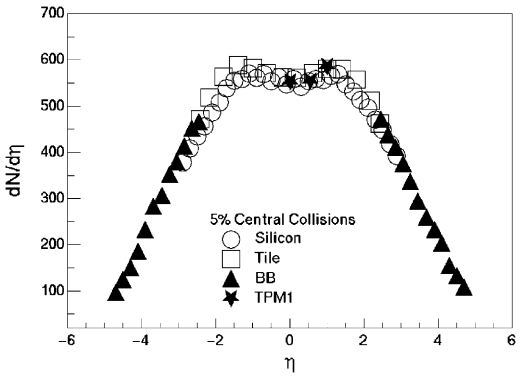

Fig. 29. Pseudo-rapidity distributions from 5% central Au+Au collisions at 130 GeV/u center of mass energy measured with the multiplicity array, BBCs and TPM1. The results from the tiles (□) are systematically higher than the Si strip data (○) in the mid-rapidity range, a feature that is not understood quantitatively. The results from TPM1 (stars) agree quite nicely with the tile and Si at the same η.

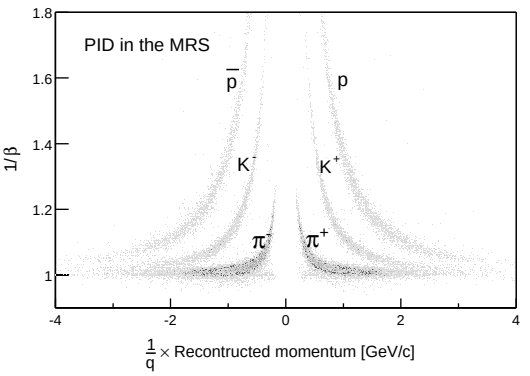

Fig. 30. TOF of charged particles in TOFW as a function of reconstructed particle momentum obtained from tracking in TPM1 and TPM2 through the D5 magnet.

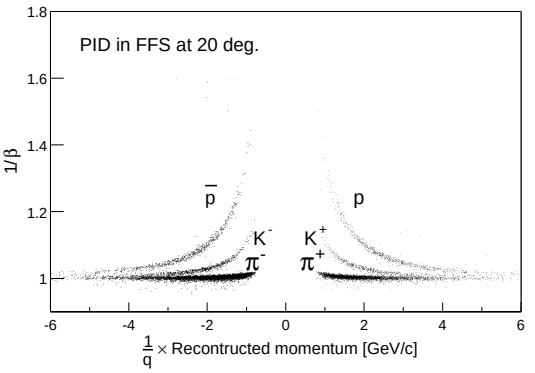

Fig. 31. TOF versus track momentum for charged particles tracked through D2 in the FFS. The TOF was measured by H1. Data for positive and negative charge are from runs with different magnet polarities added together to make one spectrum.

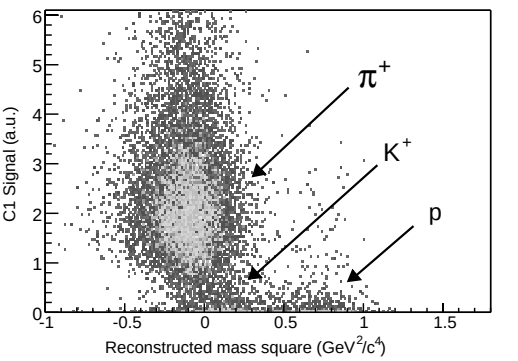

Fig. 32. C1 preliminary normalized PMT response vs. mass squared.

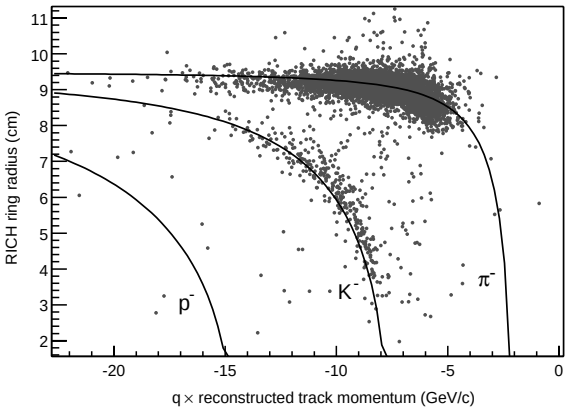

Fig. 33. Preliminary PID obtained from the RICH detector. The lines indicate the theoretical positions of the particles in the plot.

2001 RHIC run, we have begun to utilize the RICH detector. Fig. 33 shows the particle identification obtained in preliminary analysis of data collected with the RICH detector. This plot was generated projecting tracks from the DCs in the BFS into the RICH and extracting radii from PMT hits in the RICH phototubes. We observe good separation of π/K to momentum beyond 15 GeV/c. The lines in the plot indicate the positions expected for the various particles. The momentum acceptance for the setting used in that run did not allow protons to be above threshold.

8. Summary

We have presented a detail description of the BRAHMS experiment at RHIC. The physics capabilities of the device as well as the justification of choices made along with design considerations have been discussed in detail. Technical details of each of the detector subsystems are given along with a discussion of the performance of these detectors in the RHIC 2000 run as well as part of the 2001 run.

Finally we presented performance results of the different elements of the spectrometer working together. It was shown that different methods can be used to determine the vertex in the collider experiment.

Three different technologies are shown to give consistent results regarding particle multiplicity measurements over a wide range of pseudo-rapidity. These results have provided interesting physics that significantly constrains existing models [21,22].

Particle identification examples show that we can use the TOF method to separate π/K up to $p \approx 3.0$ GeV/c using H1 in the FS and up to 2.2 GeV/c in the MRS compared to the design goals of 3.3 for the FS and up to $p \approx 2.0$ GeV/c in the MRS. We also achieved K/p separation up to $p \approx 5.2$ GeV/c using H1 in the FS and up to $p > 3.5$ GeV/c in the MRS compared to the design goals of 5.7 GeV/c in the FS and 3.5 GeV/c in the MRS. In addition, the momentum range is significantly increased when the C1 and RICH detectors are used. π/K separation beyond 15 GeV/c is achieved in preliminary analysis.

In conclusion, we have shown that the performance of the spectrometer as a whole in the first RHIC run comes very close to meeting the design goals of the spectrometer. Further refinement of analyses as well as slight improvements to the various detector subsystems will allow us to meet and exceed these design specifications and in doing so exploit the unique features of BRAHMS.

Acknowledgements

The very professional efforts of the RHIC team to commission the accelerator and deliver the beams are gratefully acknowledged. This work was supported by the Division of Nuclear Physics of the Office of Science of the United States Department of Energy grants DE-FG02-99-ER41121, DE-AC02-98-CH10886 and DE-FG03-93-ER40773, DE-FG03-96-ER40981, the Danish Natural Science Research Council, the Research Council of Norway, the Jagiellonian University grants, the Korea Research Foundation, and the Romanian Ministry of Research (5003/1999, 6077/2000).

References

[1] T. Abbott, et al., Nucl. Instr. and Meth. A 290 (1990) 41.
[2] L. Ahle, et al., Nucl. Phys. A 590 (1995) 249c;
K. Shigaki, et al., Nucl. Phys. A 590 (1995) 519c;
K. Shigaki, et al., Nucl. Instr. and Meth. A 438 (1999) 282.
[3] GEANT, Detector description and simulation tool, CERN Program Library Long Writeup W5013, CERN, Geneva (1993); http://wwwinfo.cern.ch/asd/geant.
[4] C. Adler, et al., Nucl. Instr. and Meth. A 470 (2001) 488.
[5] A.J. Baltz, C. Chasman, S.N. White, Nucl. Instr. and Meth. A 417 (1998) 1.
[6] H. Appelshauser, et al., Eur. Phys. J. A 2 (1998) 383.
[7] TOSCA Reference Manual, Vector Field Limited, Oxford, England, 1992.
[8] R. Veenhof, The Garfield Program v.7.01, http://consult.-cern.ch/writeup/garfield.
[9] S. Afanasiev, et al., Nucl. Instr. and Meth. A 430 (1999) 210;
ALICE Collaboration, CERN/LHCC 2000-001 ALICE-TDR-7.
[10] S.R. Klein, et al., IEEE Trans. Nucl. Sci. NS-43 (1996) 1768.
[11] Z. Majka, et al., in preparation.
[12] F.M. Newcomer, S. Tedja, R. Van Berg, J. Van der Spiegel, H.H. Williams, IEEE Trans. Nucl. Sci. NS-40 (1993) 630.
[13] R. Debbe, et al., Nucl. Instr. and Meth. A 371 (1996) 327.
[14] T. Ypsilantis, J. Seguinot, Nucl. Instr. and Meth. A 343 (1994) 30.
[15] Micron Semiconductor Inc., 126 Baywood Avenue, Longwood, FL, USA.
[16] BICRON, 6801 Cochran Road, Solon, Ohio, USA.
[17] DuPont, P.O. Box 88, Sheridan Drive and River Road, Buffalo 14207-0088, NY.
[18] Kuraray America, Inc., 200 Park Avenue, New York 10166, NY.
[19] Kinetic Systems, Inc., 20 Arboretum Rd., Boston 02131, MA.
[20] R. Brun, F. Rademakers, Nucl. Instr. and Meth. A 389 (1997) 81.
[21] I.G. Bearden, et al., The BRAHMS collaboration, Phys. Lett. B 523 (2001) 227.
[22] I.G. Bearden, et al., The BRAHMS collaboration, Phys. Rev. Lett. 87 (2001) 112305.